Mini-symposium M1

COMPUTATIONAL BIOMECHANICS

Organizer: Nenad Filipović

MOTION OF CIRCULAR AND ELLIPTICAL PARTICLES IN LAMINAR FLOWS

V. Isailovic[1], T. Djukic[1,2], M. Ferrari[3], N. Filipovic[1,2] and M. Kojic[1,3]

[1] Bioengineering Research and Development Center, BioIRC Kragujevac
Prvoslava Stojanovica 6, 34000 Kragujevac
e-mail: velibor@kg.ac.rs
[2] Faculty of Mechanical Engineering, University of Kragujevac
Sestre Janjic 6, 34000 Kragujevac
e-mail: fica@kg.ac.rs
[3]Methodist Hospital Research Institute, Houston, USA
e-mail: mkojic@hsph.harvard.edu

Abstract. Nanotechnology with nanoparticles offers new ways in transport of drug molecules and contrast agents by the blood flow through the circulatory system. In this study, we use a finite element (FE) continuum procedure, as well as discrete dissipative particle dynamics (DPD) and Lattice Boltzmann (LB) method to model the motion of circular and elliptical particles in a 2D laminar flow. Three examples are considered: i) one sedimenting cylinder in a channel, ii) two sedimenting cylinders in a channel, and iii) motion of four ellipsoidal particles in a linear shear flow. A good agreement with solution from available literature was found. These results show that the approach with FE, as well as DPD and LB methods can effectively be applied to model motion of micro/nano-particles for drug delivery system.

1. Introduction

It is well known that the efficacy of molecule based therapies and imaging is mainly delivery limited. A multitude of barriers along the circulatory system prevent therapeutic molecules and tracers for imaging from reaching their biological target in the desired mass fractions [1]. The use of drug delivery systems have been improved the areas of cancer prevention and pain management related to classical cancer chemotherapy [2].

Nanotechnology offers opportunities to interface with biology in new ways and with unprecedented precision. The size of nanoparticles is becoming an important variable that affects the way they enter cells and how they influence the cell functions [3].

In this study we examine particle motion in a two-dimensional channel and motion of an ellipsoidal particle in a linear shear flow. Two different methodologies were implemented. The continuum strong coupling procedure for fluid-solid interaction was implemented in our in-house finite element procedure [3]. Also DPD and LB were applied for motion of an ellipsoidal particle in a linear shear flow. At the end a discussion and conclusions are presented.

2. Methods

2.1 Governing equation for fluid domain

We here give a final form of equations for fluid domain. The incremental-iterative balance equation of a finite element for a time step 'n' and equilibrium iteration 'i' has a form [3]

$$\begin{bmatrix} \frac{1}{\Delta t}\mathbf{M} + {}^{n+1}\tilde{\mathbf{K}}_{vv}^{(i-1)} & \mathbf{K}_{vp} \\ \mathbf{K}_{vp}^{T} & \mathbf{0} \end{bmatrix} \begin{Bmatrix} \Delta\mathbf{V}^{(i)} \\ \Delta\mathbf{P}^{(i)} \end{Bmatrix}_{blood} = \begin{Bmatrix} {}^{n+1}\mathbf{F}_{ext}^{(i-1)} \\ 0 \end{Bmatrix} - \begin{bmatrix} \frac{1}{\Delta t}\mathbf{M} + {}^{n+1}\mathbf{K}^{(i-1)} & \mathbf{K}_{vp} \\ \mathbf{K}_{vp}^{T} & 0 \end{bmatrix} \begin{Bmatrix} {}^{n+1}\mathbf{V}^{(i-1)} \\ {}^{n+1}\mathbf{P}^{(i-1)} \end{Bmatrix} + \begin{Bmatrix} \frac{1}{\Delta t}\mathbf{M}\,{}^{n}\mathbf{V} \\ 0 \end{Bmatrix} \tag{1}$$

where ${}^{n+1}\mathbf{V}^{(i-1)}$ ${}^{n+1}\mathbf{P}^{(i-1)}$ are the nodal vectors of blood velocity and pressure, with the increments in time step $\Delta\mathbf{V}^{(i)}$ and $\Delta\mathbf{P}^{(i)}$ (the index 'blood' is used to emphasize that we are considering blood as the fluid); Δt is the time step size and the left upper indices 'n' and 'n+1' denote start and end of time step; and the matrices and vectors are defined in [3]. The vector ${}^{n+1}\mathbf{F}_{ext}^{(i-1)}$ of external forces includes the volumetric and surface forces. In the assembling of these equations, the system of equations of the form (1) is obtained, with the the surface forces acting only on the fluid domain boundary (the surface forces among the internal element boundaries cancel).

2.2 Governing equations for solid domain

Equation of motion can be described by second order Lagrangian differential equation. The equilibrium equation at the end of time step is:

$$\mathbf{K}\Delta\mathbf{U}^{i} = \mathbf{F}^{\text{ext}} - \mathbf{F}^{\text{int}} - \mathbf{F}^{\text{in}} \tag{2}$$

where:

$\mathbf{F}^{\text{in}} = \mathbf{M}\,{}^{n+1}\ddot{\mathbf{U}}^{i}$ - is inertial force,

$\mathbf{M} = \int_{V} \rho\mathbf{H}^{T}\mathbf{H}dV$ - is mass matrix,

$\mathbf{K} = \int_{V} \mathbf{B}^{T}\mathbf{C}\mathbf{B}dV$ - is stiffness matrix,

$\Delta\mathbf{U}^{i}$ - is displacement vector,

${}^{n+1}\ddot{\mathbf{U}}^{i}$ - is acceleration vector,

$\mathbf{F}^{\text{ext}}$ - is external force vector,

$\mathbf{F}^{\text{int}}$ - is internal force vector.

We have that for the fluid domain velocities are nodal variables as can be seen from equation (1). In order to design a fully coupling procedure, we transformed the governing equation of solid (2) to velocity formulation. We consider that acceleration in time is constant and it can be described for the current time step as:

$$ {}^{n+1}\ddot{\mathbf{U}}^{i} = \frac{{}^{n+1}\dot{\mathbf{U}}^{i} - {}^{n}\dot{\mathbf{U}}}{\Delta t} \tag{3} $$

We express the displacement increment in equation (2) as:

$$ \Delta\mathbf{U}^{i} = \Delta\dot{\mathbf{U}}^{i}\Delta t \tag{4} $$

so that equation (2) becomes:

$$ \mathbf{M}\frac{{}^{n+1}\dot{\mathbf{U}}^{i} - {}^{n}\dot{\mathbf{U}}}{\Delta t} + \Delta t\mathbf{K}\Delta\dot{\mathbf{U}}^{i} = \mathbf{F}^{\text{ext}} - \mathbf{F}^{\text{int}} \tag{5} $$

Velocity in the current iteration can be written as sum of the value from the previous iteration and the current velocity increment:

$$ {}^{n+1}\dot{\mathbf{U}}^{i} = {}^{n+1}\dot{\mathbf{U}}^{i-1} + \Delta\dot{\mathbf{U}}^{i} \tag{6} $$

Now equation 2 becomes:

$$ \mathbf{M}\frac{{}^{n+1}\dot{\mathbf{U}}^{i-1} + \Delta\dot{\mathbf{U}}^{i} - {}^{n}\dot{\mathbf{U}}}{\Delta t} + \Delta t\mathbf{K}\,\Delta\dot{\mathbf{U}}^{i} = \mathbf{F}^{\text{ext}} - \mathbf{F}^{\text{int}} \tag{7} $$

Finally, we keep all the terms with the velocity increment $\Delta\dot{\mathbf{U}}^{i}$ on the left hand side, and the rest (as the force terms) write on the right hand side. The incremental-iterative balance equation of a solid finite element is:

$$ \left(\frac{\mathbf{M}}{\Delta t} + \Delta t\mathbf{K}\right)\Delta\dot{\mathbf{U}}^{i} = \mathbf{F}^{ext} - \mathbf{F}^{\text{int}} - \frac{\mathbf{M}}{\Delta t}\left({}^{n+1}\dot{\mathbf{U}}^{i-1} - {}^{n}\dot{\mathbf{U}}\right) \tag{8} $$

Note that the solution depends on the right hand side where the force terms are properly calculated. The matrices on the left hand side affect the convergence rate only, hence the multiplication factor Δt for the stiffness matrix increases the solution convergence. We used Total Lagrangian formulation for evaluating of the internal forces and stiffness matrix.

Two different meshes are generated for the fluid and solid domains, with the common nodes at the solid-fluid interface. Element balance equations (1) and (8) are assembled into one system of equations and solved for the increments of nodal velocities. A remeshing procedure was adopted and new fluid mesh is generated after a number of time steps - when the overall increments of solid displacement over these steps become large.

2.3 General equations for DPD method

In the dissipative particle dynamics (DPD) model a fluid is discretized into a set of interacting particles. Each DPD particle represents a cluster of MD particles (atoms or molecules). There exists a mass fluctuation since MD particles can enter and go out from a Voronoi cell used to discretize the fluid space. Also, the shape of the cells changes as the cells move. However, this mass fluctuation and change of shape are neglected in the DPD formulation particles. Hence, the DPD particles representing the Voronoi cells have constant mass during motion.

The evolution of the particle position, $\mathbf{r}_i$, can be obtained by application of the Newton second law:

$$\begin{aligned} \dot{\mathbf{r}}_i &= \mathbf{v}_i \\ \dot{\mathbf{v}}_i &= \frac{1}{m_i}\sum_{j\neq i}^{N}\hat{\mathbf{F}}_{ij} = \sum_{j\neq i}^{N}\mathbf{F}_{ij} \end{aligned} \tag{9}$$

where $\mathbf{v}_i$ is the particle velocity, m_i is the particle mass; $\hat{\mathbf{F}}_{ij}$ is the total force on particle i due to particle j, while $\mathbf{F}_{ij}$ is this force per unit mass; and the dot indicates a time derivative. In our analysis we assume that each particle has the same mass. Here, we have neglected the external forces for simplicity.

The interaction forces can be represented as the sum of three forces [4]: conservative (repulsion) $\mathbf{F}_{ij}^{C}$, dissipative $\mathbf{F}_{ij}^{D}$, and random force $\mathbf{F}_{ij}^{R}$,

$$\mathbf{F}_{ij} = \mathbf{F}_{ij}^{C} + \mathbf{F}_{ij}^{D} + \mathbf{F}_{ij}^{R} \tag{10}$$

These forces can expressed as:

$$\begin{aligned} \mathbf{F}_{ij}^{C} &= a_{ij}(1 - r_{ij}/r_c)\mathbf{r}_{ij}^{0} \\ \mathbf{F}_{ij}^{D} &= -\gamma w^{D}(\mathbf{v}_{ij}\cdot\mathbf{e}_{ij})\mathbf{r}_{ij}^{0} \\ \mathbf{F}_{ij}^{R} &= \sigma w^{R}\xi_{ij}\mathbf{r}_{ij}^{0} \end{aligned} \tag{11}$$

Here, a_{ij} is the maximum repulsion force per unit mass, r_{ij} is the distance between particles i and j, $\mathbf{r}_{ij}^{0} = \mathbf{r}_{ij}/r_{ij}$ is the unit vector pointing in direction from j to i, γ stands for the friction coefficient, and σ is the amplitude of the random force. Also, w^{D} and w^{R} are the weight functions for dissipative and random forces, dependent on the distance r from the particle i; and ζ_{ij} is a random number with zero mean and unit variance. The domain of influence of the interaction forces is r_c, hence $F_{ij} = 0$ for $r_{ij} > r_c$

2.4 LB Method

The equation that represents the *LB* numerical scheme and which is implemented in all the solvers based on *LB* method is given by:

$$f_i\left(\mathbf{x}+\mathbf{v}_i,t+1\right)-f_i\left(\mathbf{x},t\right)=-\frac{1}{\tau}\left(f_i\left(\mathbf{x},t\right)-f_i^{(0)}\left(\rho,\mathbf{u}\right)\right)+\left(1-\frac{1}{2\overline{\tau}}\right)F_i \tag{12}$$

In the method implementation, this equation is solved in two distinct steps: *collision step* and *propagation step* [5]. With f_i^{in} and f_i^{out} are defined the values of discretized distribution function f_i before and after the collision. f_i^{out} is at the same time the value of distribution function that represents "input data" for the next time step. τ and $\overline{\tau}$ are the relaxation time parameters [5].

The mentioned steps are now given by:

collision:

$$f_i^{out}\left(\mathbf{x},t\right)=f_i^{in}\left(\mathbf{x},t\right)-\frac{1}{\tau}\left(f_i^{in}\left(\mathbf{x},t\right)-f_i^{(0)}\left(\rho,\mathbf{u}\right)\right)+\left(1-\frac{1}{2\overline{\tau}}\right)F_i \tag{13}$$

propagation:

$$f^{in}{}_i\left(\mathbf{x}+\mathbf{v}_i,t+1\right)=f_i^{out}\left(\mathbf{x},t\right) \tag{14}$$

3. Results

We firstly performed simulation with DPD and LB of flow around cylinder of a radius R which is moving in a stagnant fluid with relative velocity V. Analytical solution for the drag force F is equal:

$$\mathbf{F}=-C_D\pi\rho R^2\left|\mathbf{V}\right|\mathbf{V} \tag{15}$$

where C_D is the drag coefficient. For Reynolds number Re, the drag coefficient is $C_D=\frac{24}{R_e}(1+\frac{3}{16}R_e)$ [6] and Eq. (15) reduces to

$$\mathbf{F}=6\pi\mu RV\left(1+\frac{3}{8}R_e\right) \tag{16}$$

Two-dimensional system of DPD and LB particles were used for calculating the drag force, where the fluid flows around stationary circular cylinder located at the center of the simulation box. A constant force is applied to all fluid particles. The height of the

simulation box is 40 times larger than the diameter of the disk. Periodic boundary conditions are used for the input and output. There is no motion of the particles at the channel walls and those used to model the rigid cylinder.

The circular cylinder is modeled as freezing group of the DPD and LB particles. The total force on the circular cylinder is calculated as a sum of all DPD or LB forces on the freezing particles inside the cylinder. The linearity of the mean drag force and radius can be observed from Fig.1 which corresponds to Stokes (Oseen) regime and the analytical solution for drag force [6].

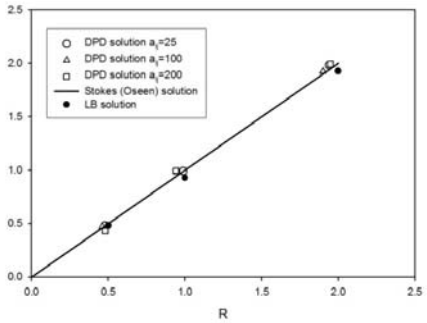

Figure 1. Drag force as function of circular cylinder radius R

The next example is related to the motion of one sedimenting cylinder in a channel shown in Fig.2. [7]. We used strong coupling finite element procedure to solve this problem. The width of the channel is 4d, where d=0.5cm is the diameter of the cylinder. The cylinder starts at the center of the channel. The height of the channel is 50 cm. The cylinder is falling under the gravity force. The density of the fluid is $\rho=1 g/cm^3$ and dynamic viscosity is 1.0e-2 g/(cm s).

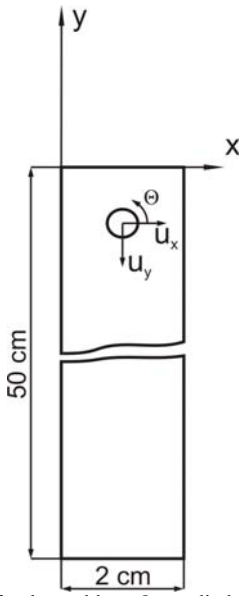

Figure 2. Basic geometry data for the problem. One cylinder sedimenting in a channel

Displacements in time for X and Y directions are presented in Figs 3a and 3b respectively. Also velocity distribution in X and Y direction as well as angle and angular velocity are shown in Figs. 3c,3d,3e and 3f respectively. From these figures it can be seen that dominant motion is the periodic oscillation which is associated with vortex shedding behind the cylinder. Velocity distributions for one, two cylinders and four ellipsoids sedimenting in a channel are presented in Fig. 4. These results are in good agreement with [7].

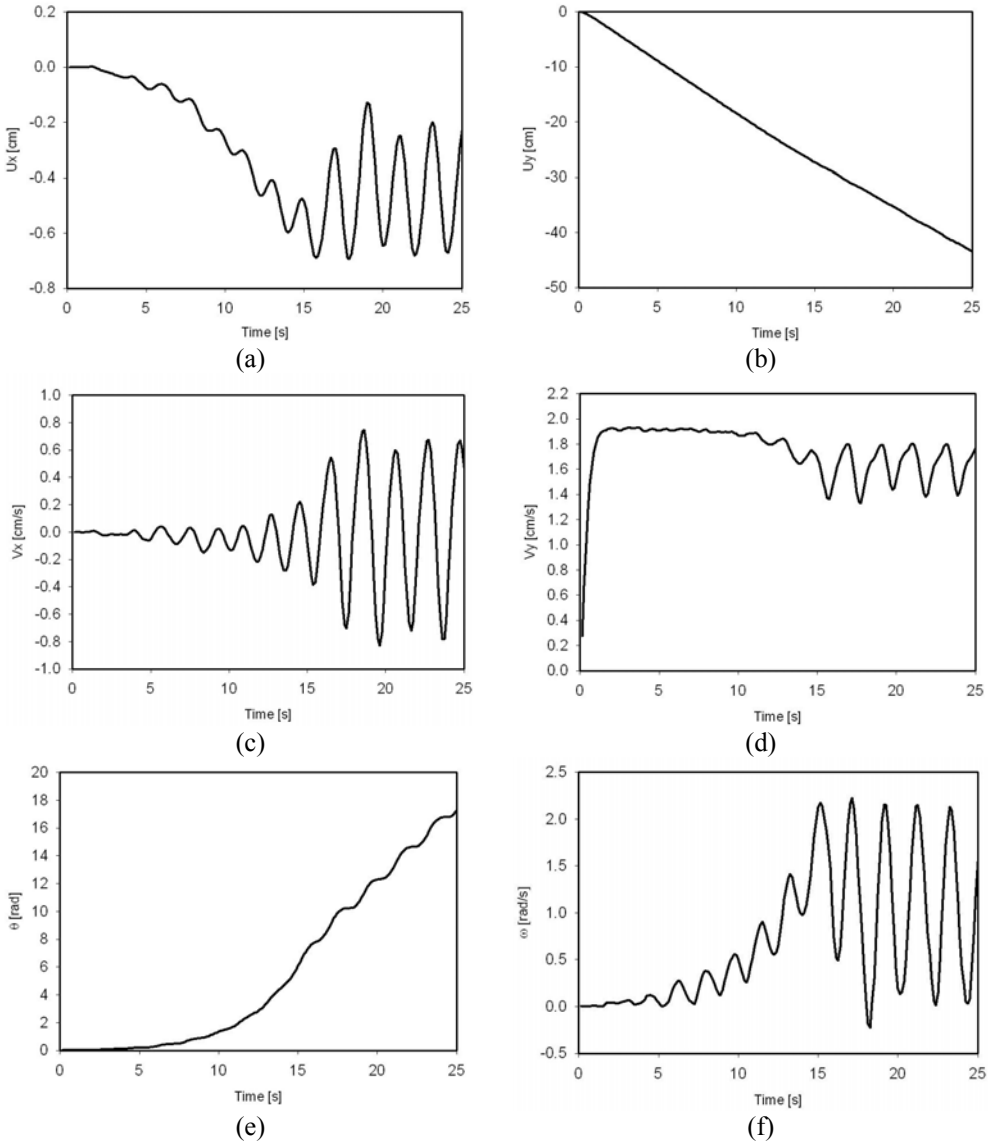

Figure 3. A sedimenting cylinder in a channel. The diameter of the cylinder is d=0.5cm, the width of the channel is 2cm. The cylinder starts at the center of the channel. Displacements and velocity of the cylinder in X and Y direction are shown in (a),(b), (c) and (d), angle and angular velocity versus time are shown in (e) and (f), respectively.

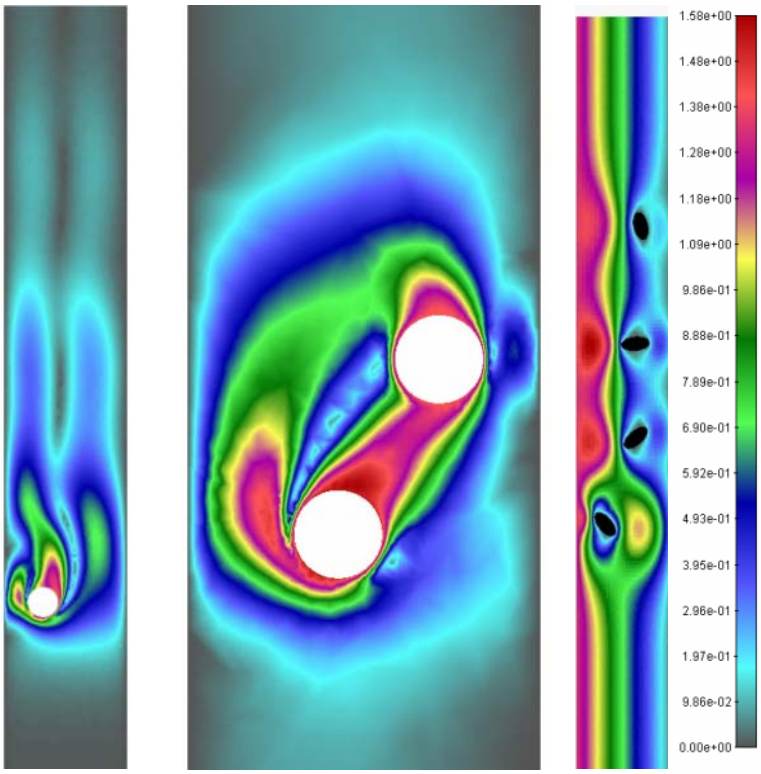

(a) (b) (c)

Figure 4. Velocity distribution for one cylinder (a), two cylinders (b) and four elliptical particles (c) sedimenting in a channel. The diameter of cylinders is d=0.5cm, diameters of the ellippse are a=0.5cm, b=0.25cm, and the width of the channel is 2 cm.

In the following example, the motion of an elliptical particle in a linear laminar flow was analyzed by finite element (FE) and DPD methods. This motion was firstly predicted by Gavze and Shapiro [7-9] using a boundary element formulation and recently more deeply analyzed by the group of Decuzzi [10,11] using a semi-analytical approach combined with a finite element analysis.

The fluid domain was discretized into finite elements, with geometry and boundary conditions as shown in Fig.5; where H is the channel height, L is the channel length, b_1 and b_2 are the major and minor semi-length axes of ellipsoidal particle, y_0 is the initial separation distance from the wall, and θ_0 is initial angle between the major axis of the particle and the flow direction.

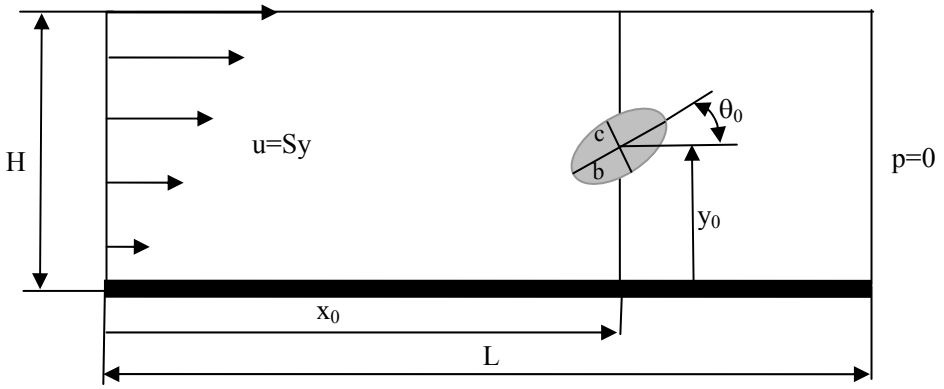

Figure 5. Geometrical data and boundary conditions of the model for motion of elliptical particle within a shear creeping flow

Particle trajectory, normalized with respect to the ellipse dimension *c*, is shown in Fig.5 by solid line, for the Stokes number St =0.125. As can be seen, the trajectory has an oscillatory character, with particle moving toward the wall and then away from the wall, with the closest position corresponding to angle $\theta = 0$ (larger axis parallel to the wall).

For the DPD model, a 2D system containing 5000x500 DPD beads was considered. The DPD particle distribution corresponds to the number density n = 4 and the average distance between beads is $\lambda = 1/3$. The DPD particles at the wall were assumed frozen as well as particles inside the elliptic rigid particle. A linear shear flow was generated by applying a shear external force on the fluid DPD particles. The DPD parameters for fluid-fluid particles (see equation (11)) were: a_{ij} =25k_BT, γ =4.5k_BT, with k_BT is assumed to be equal unity. Fluid-particle interaction parameter was set to a_{ij} = 100 k_BT/ρ. A constant time step Δt=2x10^{-4} (DPD time) was used for this simulation. The DPD solution for the particle center trajectory is shown in Fig. 6. It can be seen that the DPD trajectory has some deviation from the FE solution, but the two trajectories have the same character.

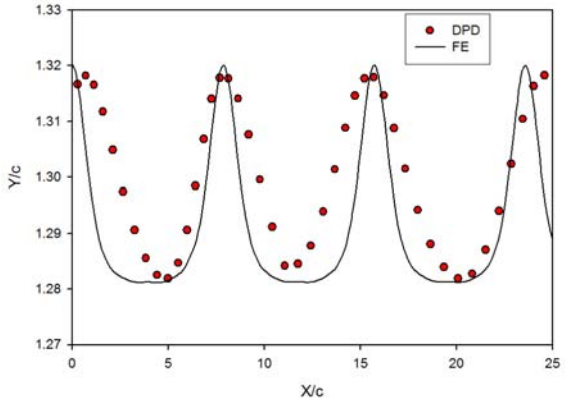

Figure 6. The trajectory of elliptical particle in a linear laminar flow with $\theta_0 = \pi/2$ in the absence of gravitational force. FE solution with *St*=0.125, DPD solution with shear external force F_x=1

4. Discusion and conclusions

A particle motion problem within microchannels was investigated. We examined motion of one and two sedimenting cylinders, and four elliptical particles, in a channel; also, we calculated trajectory of one and four elliptical particles in a linear laminar flow. A strong coupling procedure for both domains solid and fluid was implemented within finite element method. Also discrete method DPD and LB were implemented to calculate drug force acting on a fixed cylinder in a laminar flow.

We found good agreement between our results and those available in literature for a sedimenting cylinder in a vertical channel. Also interaction between two cylinders and four ellipses shows drafting, kissing and tumbling which are a local rearrangement mechanism in a two-phase flow of solids and liquids in beds of particles confined to move in two dimensions. Agreement between the DPD, LB and analytical or FE solutions demonstrate that these methods can be used to model complex problems of fluid flow and fluid-solid interaction in microfluidics. These features are of particular interest in biomedical sciences, for investigations of blood flow within microvessels, cell or particle transport and margination to the vessel walls and drug delivery.

Acknowledgments

This work was supported in part by Ministry of Science in Serbia, Grant ON174028 and III41007 and by a Grant from BioIRC- The Methodist Hospital Research Institute, Houston.

References

[1] Reiner Z, Dominik R, Iduna F. (2004) Reduction of tamoxifen resistance in human breast carcinomas by tamoxifen-containing liposomes, *in vivo*. *Anti-Cancer Drugs* Vol 15, pp 707-714.
[2] Decuzzi P., Causa F., Ferrari M., Netti P.A., (2006) The effective dispersion of nanovectors within the tumor microvasculature, *Ann Biomed Eng.* Vol 34, pp 633-41.
[3] Kojic M., Filipovic N., Stojanovic B., Kojic N., (2008) *Computer Modeling in Bioengineering: Theoretical Background, Examples and Software*, John Wiley and Sons, Chichester, England
[4] Espanol P and Warren PB (1995) Statistical mechanics of dissipative particle dynamics, *Europhys. Lett*. Vol 30, pp 191-196.
[5] Hatzikirou H., Brusch L., Schaller C., Simon M., Deutsch A. (2010) Prediction of traveling front behavior in a lattice-gas cellular automaton model for tumor invasion, *Computers and Mathematics with Applications*, 59 (7), pp. 2326-2339.
[6] Chwang AT and Wu TY (1974) Hydromechanics of low-Reynolds-number flow. Part 4. Translation of spheroids, *J. Fluid Mech.* 75(4), 1976,:677-689.
[7] Hu Howard and Joseph Daniel, (1992) Direct simulation of fluid particle motion, *Theoretical and Computational Fluid Dynamics* Vol 3, pp 285-306.
[8] Gavze E and Shapiro M (1997) Particles in a shear flow near a solid wall effect of nonsphericity on forces and velocities, *Int. J. Multiphase Flow*. Vol 23(1), pp 155-182.
[9] Gavze E and Shapiro M (1998) Motion of inertial spheroidal particles in a shear flow near a solid wall with special application to aerosol transport in microgravity, *J. Fluid Mech*. Vol 371, pp 59-79.
[10] Decuzzi P, Lee S, Bhushan B, Ferrari M (2005), Theoretical model for the margination of particles within blood vessels, *Ann. Biomed. Eng*. Vol 32(6), pp 793-802.
[11] Decuzzi P, Ferrari M (2006), The adhesive strength of non-spherical particles mediated by specific interactions, *Biomaterials,* Vol 27(30), pp 5307-14.

SIMULATION OF THE CONDITIONS LEADING TO DUODENAL STUMP DISRUPTION AFTER BILLROTH II GASTRIC RESECTION

D. Milasinovic[1], A. Cvetkovic[2], N. Filipovic[1,3]and M. Kojic[1,4]

[1]Bioengineering Research and Development Center, BioIRC Kragujevac
Prvoslava Stojanovica 6, 34000 Kragujevac
e-mail: dmilashinovic@kg.ac.rs
[2]Medical Faculty Kragujevac, University of Kragujevac
Svetozara Markovica 69, 34000 Kragujevac
e-mail: alex777yu@yahoo.com
[3] Faculty of Mechanical Engineering, University of Kragujevac
Sestre Janjic 6, 34000 Kragujevac
e-mail: fica@kg.ac.rs
[4]Methodist Hospital Research Institute, Houston, USA
e-mail: mkojic@hsph.harvard.edu

Abstract. In this study Computational Fluid Dynamics (CFD) examination of how geometry of reconstructed gastrointestinal truct can influence the postoperative results of gastric resection is presented. Three-dimensional computer simulation is used in order to perform virtual gastric resection and investigate conditions at the duodenal stump after Billroth II gastric resection which may cause duodenal stump blowout. Initial finite element model of preoperative gastroduodenal region was created using data from Multi Slice Computer Tomography (MSCT). We performed virtual gastric resection using the preoperative Finite Element (FE) model and three cases after Billroth II gastric resection. CFD calculation was performed employing these models with initial simulation parameters according to our previous investigation. We calculated pressure and velocitydistributions, as well as salivaand pancreatic juice and bile concentrations. This study offers an insight into the processes within the duodenal stump after surgical intervention, which can be useful for patient-specific predictions of a surgical outcome.

1. Introduction

During recent years we became witnesses that surgical simulation has evolved from educational to even patient specific predictive tool. Cooperation between surgeon and engineer is becoming so intensive and natural that we need a new generation of stuff, educated in both professions, able to synthesize knowledge from both engineering and medicine [1]. Using well known methods of mechanical engineering, informatics and computer graphics, surgeons improve results in their fields, making surgical interventions safer and easier. First steps were made in some disciplines that consider reconstruction of hard tissues, like bones, in disciplines like orthopedic surgery, maxillophacial surgery, etc. [2][3]. We tried to show advantages of cooperation between surgeon and engineer in the field of gastrointestinal surgery, using complex three-dimensional simulation, in regard to real anatomical and physiological state in human body.

The duodenum is a short but complex and functionally highly specialized part of the small intestine with motor, sensitive and secretory functions. The length of duodenum is about 30cm and it connects stomach with the rest of the small intestine. Transit of chyme through the duodenum is a complicated process (influenced by intestinal peristalsis, gastric emptying, and pyloric sphincter tone) and is regulated by many neurological and hormone-dependent feedback mechanisms [4-8].
The peristaltic movements of duodenum are complex. Two layers of smooth muscle cells (inner-longitudinal and internal-circumferential), as well as two neurological intramural networks (Auerbach's and Meisner's complexes), are responsible for gastroduodenal peristalsis. Electrical activity of the smooth muscle cell syncytium of the duodenum and in other parts of the gastrointestinal tract is represented by two basic types of electrical waves: slow waves and the spikes. Slow waves represent basic electrical activity caused by activity of the Na-K pump. When the resting membrane potential becomes less negative than -40 mV, the spikes appear on the top of slow waves with a frequency of 1-10 Hz, and cause smooth muscle contraction. The number of duodenal contractions is about 12/min[9]. Several new investigations suggest that slow waves and spikes are regulated and spread through different cell networks[10].
Dysfunction of the duodenum can occur as a result of many disorders of gastric emptying and dyspeptic complaints, which demonstrates very important role of the duodenum[11]. It becomes especially apparent after surgical interventions on the gastroduodenum[12,13].

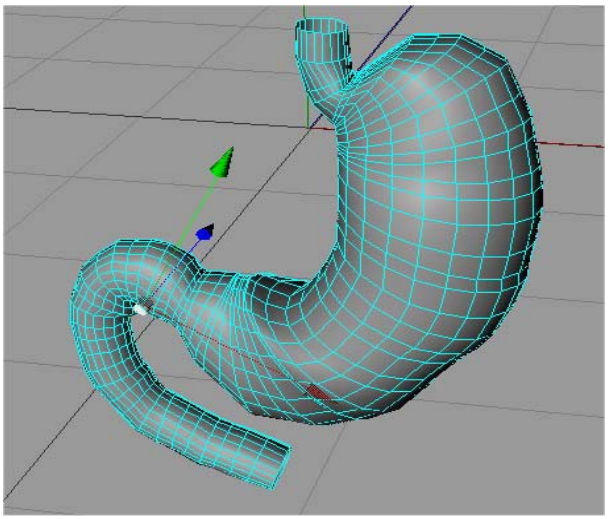

Figure 1. Preoperative state of gastroduodenal region

A large number of studies have investigated the intact gastrointestinal tract anatomically[14-16], but there have been relatively few studies on the consequences of cutting muscles, nerves and other important anatomical structures of the gastroduodenum. These cuttings are unavoidable during surgical interventions, with disturbance of many fine, highly sophisticated feedback systems. Those undesirable conditions lead to negative feedback mechanisms[17,18] that cause changes in physiological processes with respect to the preoperative state[19,20].

Insufficient attention has been paid to how the changes of geometry and flow on reconstructed gastroduodenal region affect possible postoperative complications after distal gastric resection. There are various types of reconstruction of gastrointestinal continuity after gastric resection. During recent years, three basic types have become more frequent. The first and most physiological variant is a state in which continuity of the gastrointestinal tract is reconstructed with anastomosis between the gastric stump and the duodenum; this procedure is called Billroth I gastric resection (gastroduodenal anastomosis). The other type of reconstruction is the Billroth II operation, which is shown in Figure 2, in which the anastomosis is located between the gastric stump and a loop of jejunum (gastrojejunal anastomosis, gut to side), and this type of intervention is the subject of our study. The length of the proximal jejunal loop is variable and depends on anatomical variations (e.g. length of the mesenterium of the small intestine, and adhesions), as well as surgeons' ability. The jejunal loop conducts duodenal juice toward the gastric stump and the rest of the intestine. There is a hypothesis that increased intraluminal pressure in the afferent loop is the dominant cause of duodenal suture dehiscence (caused by the length of afferent jejunal loop, narrow gastrojejunoanastomosis, etc [21-23]). The distal or efferent loop is the part of the duodenum that is downstream of the anastomosis, and it conducts duodenal and gastric stump content distally to the small intestine. The anastomosis is antecolic when the jejeunal loop is positioned in front of the transverse colon, or the jejunal loop may be brought up posteriorly through an opening made in the transverse mesocolon (retrocolic anastomosis). Adequate position, shape and diameter of the anastomosis facilitate gastric emptying. The orientation of the jejunal loop may be two-fold, isoperistaltic, when the stomach and jejunum have the same peristalsis direction, and antiperistaltic, when the stomach and afferent loop of the jejunum have the opposite direction of peristalsis.

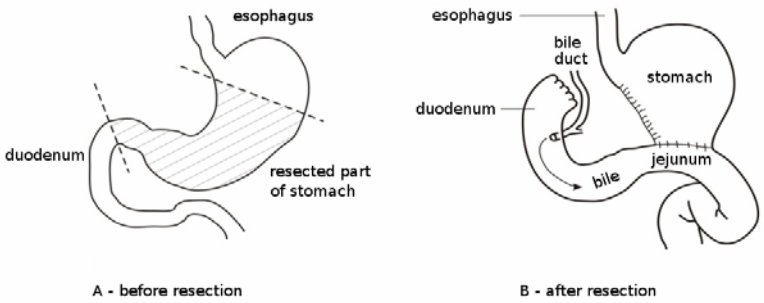

Figure 2. Schematic representation of reconstruction of gastrointestinal continuity after gastric resection. A: Normal anatomy of gastroduodenal region with resection lines; B: Billroth II anastomosis.

There are other methods of gastrointestinal tract reconstruction after gastric resection, and one of these is called Roux en Y gastrojejunoanastomosis, in which the small bowel is cut distal to the ligament of Treitz, and the anastomosis is created between the distal limb of the jejunum and remaining gastric tissue (or esophagus in cases of total gastrectomy). The proximal limb of the jejunum is positioned downstream to the jejunum at a distance of about 45 cm, where a termino-lateral end-to-side anastomosis is created[24,25].
In gastrointestinal tract reconstruction, the small bowel is not prepared to receive acidic content from the stomach, especially when duodenal juice is not present to neutralize it[26]. Suture dehiscence with postoperative peritonitis can occur as a complication after surgical intervention. Duodenal stump blowout is considered as a serious postoperative

complication, with high mortality rate[27,28]. Suture dehiscence after surgical intervention in the gastroduodenal region has been the subject of many investigations, but still many pathological mechanisms involved in this surgical problem remain unclear[29].
This study offers a new approach to this problem. Using finite element analysis with computer modeling and clinical experiments and data obtained from MSCT we attempted to determine physiological constants relevant to the above-mentioned surgical complication. In order to achieve this goal, we computed extreme increasing of pressure in the duodenal stump after distal gastric surgical resection and a Billroth II procedure, considering characteristics of suture material, characteristics of chime, etc. Three different cases with a slightly different geometrical connection of the duodenal and gastric parts during gastric resection are analysed.

2. Methods

We have used data obtained from MSCT and created initial patient specific 3D model using in house software that we created for that purpose. Then we performed virtual surgical intervention and created several postoperative models with a slightly different geometries of the same reconstruction technique. We created several variants of postoperative model in order to investigate influences of pressure distribution in the duodenal stump which may lead to disruption at the suture area. This modeling technique can be used in future in order to compare different types of surgical reconstruction after distal gastric resection.
A computational analysis taken in this study is used to examine several different Billroth II antiperistaltic anastomosis cases. A viscous incompressible fluid flow is considered as model for the transit of chyme. This flow is governed by the Navier-Stokes equations and continuity equation that can be written as [30-31].

$$\rho\left(\frac{\partial v_i}{\partial t}+v_j\frac{\partial v_i}{\partial x_j}\right)=-\frac{\partial p}{\partial x_i}+\mu\left(\frac{\partial^2 v_i}{\partial x_j\partial x_j}+\frac{\partial^2 v_j}{\partial x_j\partial x_i}\right) \tag{1}$$

$$\frac{\partial v_i}{\partial x_i}=0 \tag{2}$$

wherev_i is the chyme velocity in direction x_i, ρ is the fluid density, p is pressure, μ is the dynamic viscosity; and summation is implied on the repeated (dummy) indices, i,j=1,2,3. The first equation represents balance of linear momentum, while the equation (2) expresses incompressibility condition.
To take into account mass transport of salive, pancreatic juice and bile, we use the additional transport equation. The assumption is that the concentration of these juices does not affect the fluid gastric flow (i.e. a diluted mixture is considered). The mass transport process is governed by the convection-diffusion equation,

$$\frac{\partial c}{\partial t}+v_x\frac{\partial c}{\partial x}+v_y\frac{\partial c}{\partial y}+v_z\frac{\partial c}{\partial z}=D\left(\frac{\partial^2 c}{\partial x^2}+\frac{\partial^2 c}{\partial y^2}+\frac{\partial^2 c}{\partial z^2}\right) \tag{3}$$

where*c* denotes the juice concentration; v_x , v_y v_z are the gastric velocity components in the coordinate system *x*, *y*, *z*; and *D* is the diffusion coefficient, assumed constant, of the transported juice.

The code was validated using the analytical solution for shear stress and velocities through straight tube [30]. The finite element equations are solved with respect to velocities after the pressure was eliminated by a so-called penalty procedure. The solution is obtained by use of an incremental-iterative approach and implicit integration scheme over time. The system of algebraic equations of balance for a finite element, and for a time step and equilibrium iteration "*m*", can be written as:

$$\begin{bmatrix} \frac{1}{\Delta t}\mathbf{M}_{\mathbf{v}} + {}^{t+\Delta t}\mathbf{K}_{\mathbf{vv}}^{(m-1)} + {}^{t+\Delta t}\mathbf{K}_{\mu\mathbf{v}}^{(m-1)} + {}^{t+\Delta t}\hat{\mathbf{K}}_{\mu\mathbf{v}}^{(m-1)} + {}^{t+\Delta t}\mathbf{J}_{\mathbf{vv}}^{(m-1)} + \mathbf{K}_{\lambda\mathbf{v}} & \mathbf{0} \\ {}^{t+\Delta t}\mathbf{K}_{cv}^{(m-1)} & \frac{1}{\Delta t}\mathbf{M}_c + {}^{t+\Delta t}\mathbf{K}_{cc}^{(m-1)} + {}^{t+\Delta t}\mathbf{J}_{cc}^{(m-1)} \end{bmatrix} \begin{Bmatrix} \Delta\mathbf{v}^{(m)} \\ \Delta c^{(m)} \end{Bmatrix} = \begin{Bmatrix} {}^{t+\Delta t}\hat{\mathbf{F}}_{\mathbf{v}}^{(m-1)} \\ {}^{t+\Delta t}\mathbf{F}_c^{(m-1)} \end{Bmatrix} \quad (4)$$

where the detailed expressions for the matrices and vectors can be found elsewhere (e.g.[30-31])

3. Results

The rate of postoperative gastric resection complication seems to be primarily influenced by increased duodenal pressure. Localization and extent of the malignant process, suture material, surgical technique, presence of potentially pathogenic microorganisms colonizing the digestive tract, and tissue quality, also may play a role in the pathogenesis of this complication[32,33]. In this study, we focused on numerical simulation et gastroduodenal region after Billroth II gastric resection. We compared cases with a slightly different geometrical connection of the duodenal and gastric parts during gastric resection. In this study three cases A, B and C are presented. Case A is the least favorable because of long afferent loop and negative angle between gastric stump and jejunum. Case B has average length of afferent loop, in this case gastric stump and jejunum are connected horizontally. Case C has the shortest afferent loop and also horizontally connection of the gastric stump and jejunum. Pressure and velocity distributions at steady state flow conditions for these three cases have been shown in Figs. 3a,b,c and Figs. 4a,b,c respectively. Mass transport distributions for saliva and pancreatic juice and bile are presented in Figs 5a,b,c and Figs 6a,b,c respectively.

As expected, the maximum pressure was localized in the duodenal suture area. The results of this analysis implied that case C was more favorable with respect to juice transport because of continual juices distribution and an empty duodenal section. Comparison of models with different lengths of afferent loops, as well as different types of gastrointestinal anastomosis showed that the afferent loop syndrome was an important factor in postoperative complications.

The case C is the most preferable, with short afferent loop and orientation of anastomosis plate that both facilitate fluid to stream from gastric stump right to efferent loop, as well as

good empting of afferent loop that should disable increasing of pressure inside of afferent, blind duodenal loop, and that way disable anastomosis leakage or duodenal stump disruption..

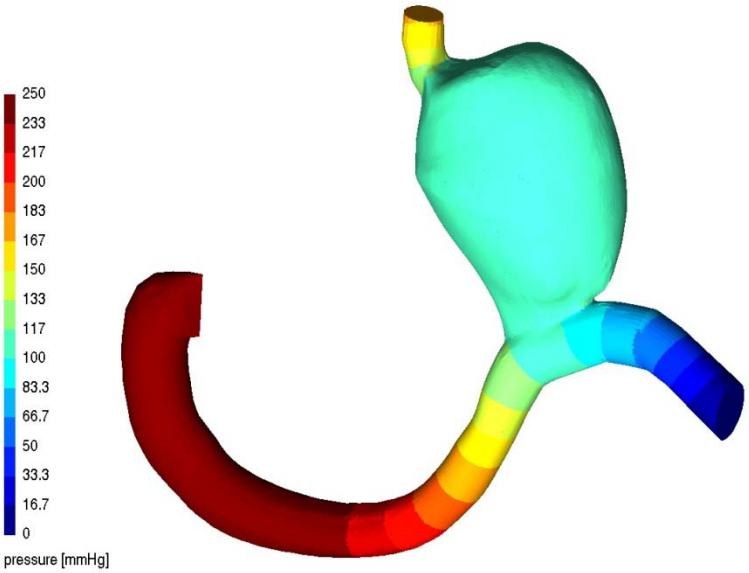

Figure 3a. Pressure distribution for the steady state flow conditions - CASE A

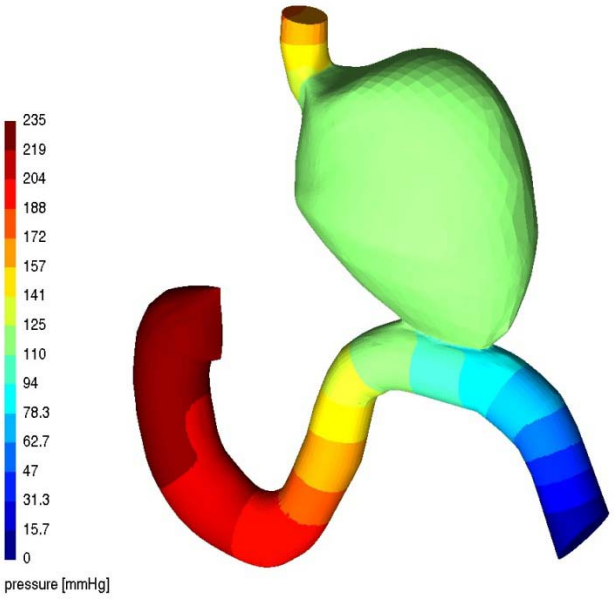

Figure 3b. Pressure distribution for the steady state flow conditions - CASE B

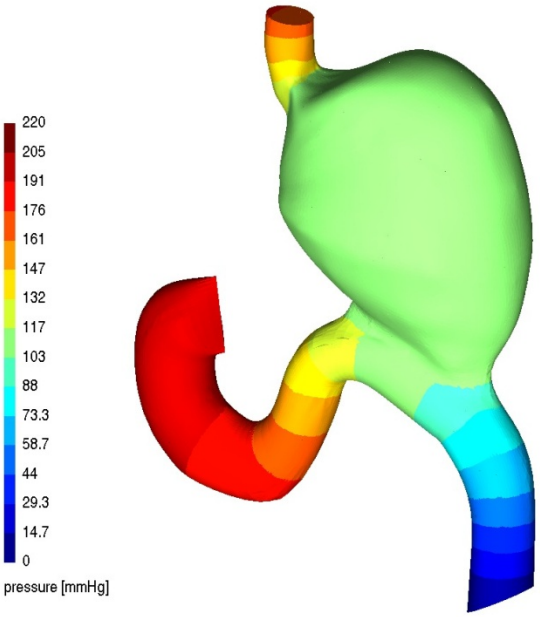

Figure 3c. Pressure distribution for the steady state flow conditions - CASE C

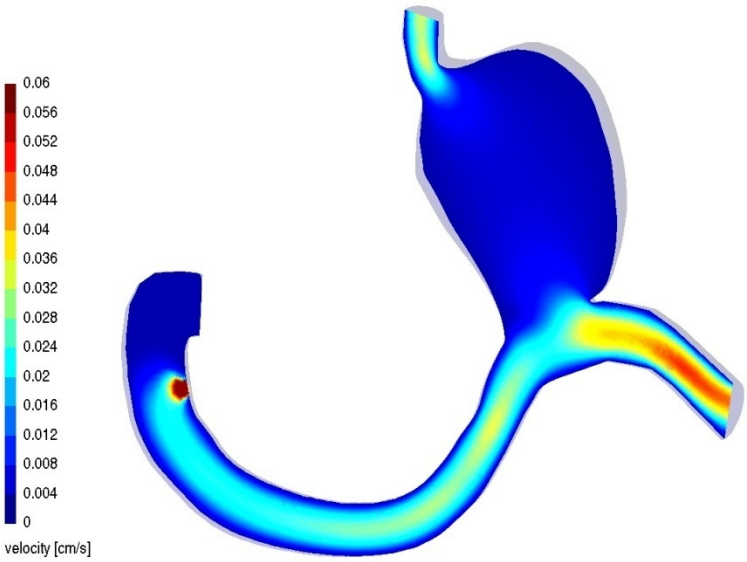

Figure 4a. Velocity distribution for the steady state flow conditions - CASE A

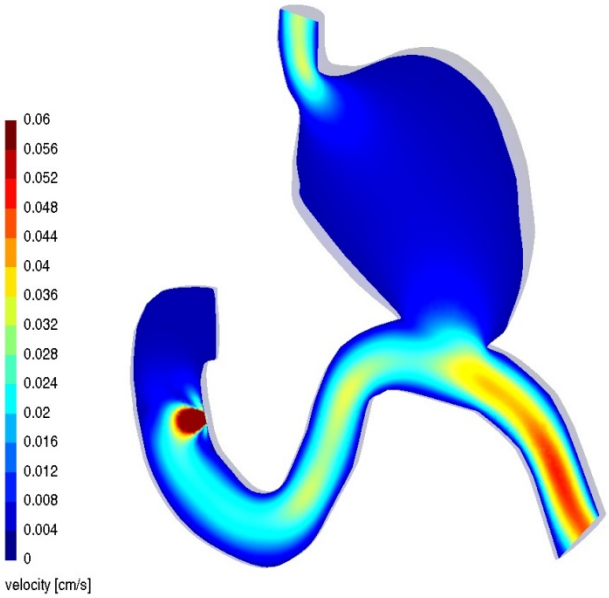

Figure 4b. Velocity distribution for the steady state flow conditions - CASE B

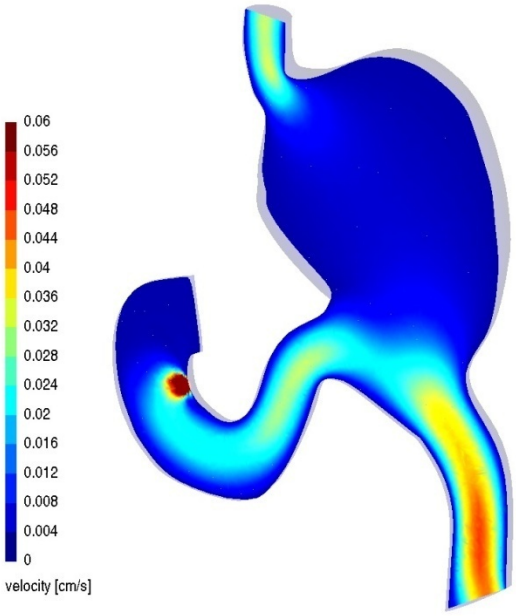

Figure 4c. Velocity distribution for the steady state flow conditions - CASE C

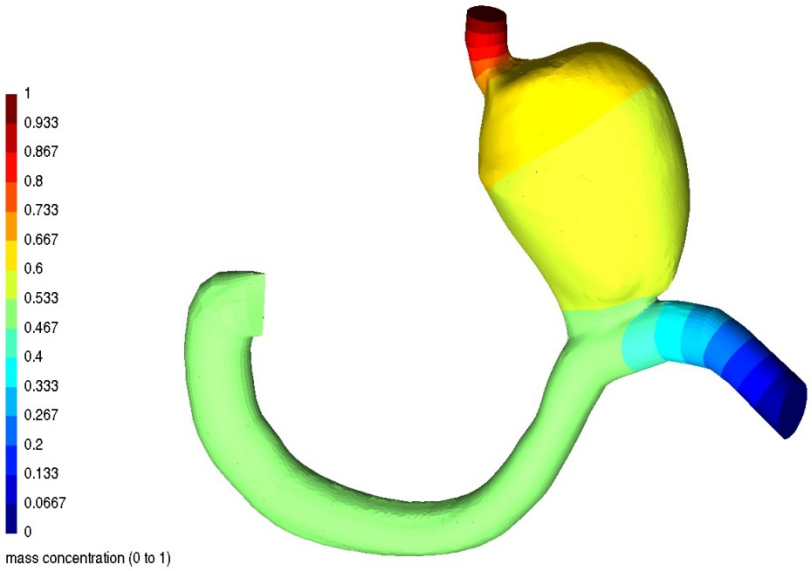

Figure 5a. Mass concentration distribution for saliva - CASE A

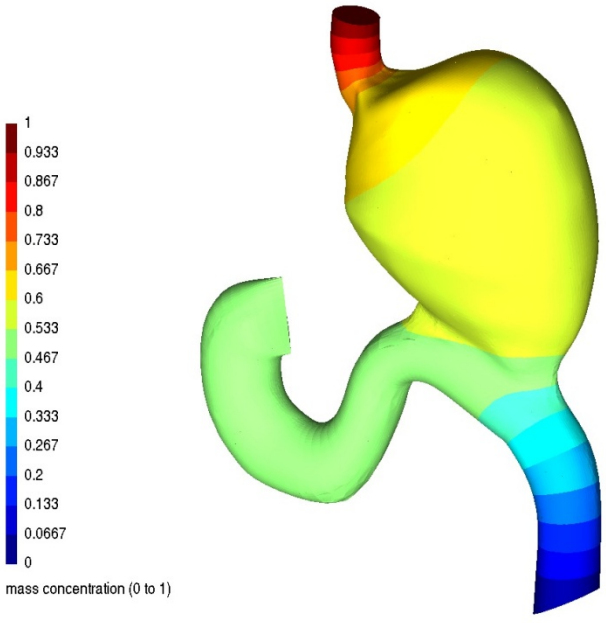

Figure 5b. Mass concentration distribution for saliva - CASE B

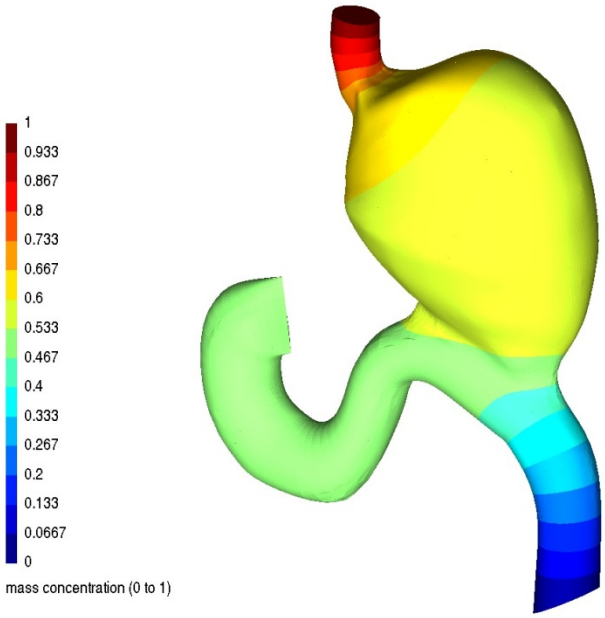

Figure 5c. Mass concentration distribution for saliva - CASE C

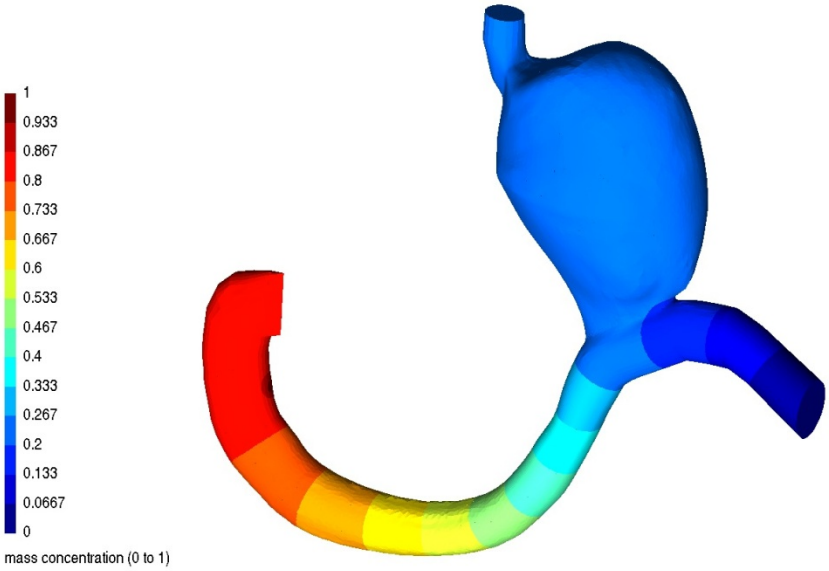

Figure 6a. Mass concentration distribution for pancreatic juice and bile - CASE A

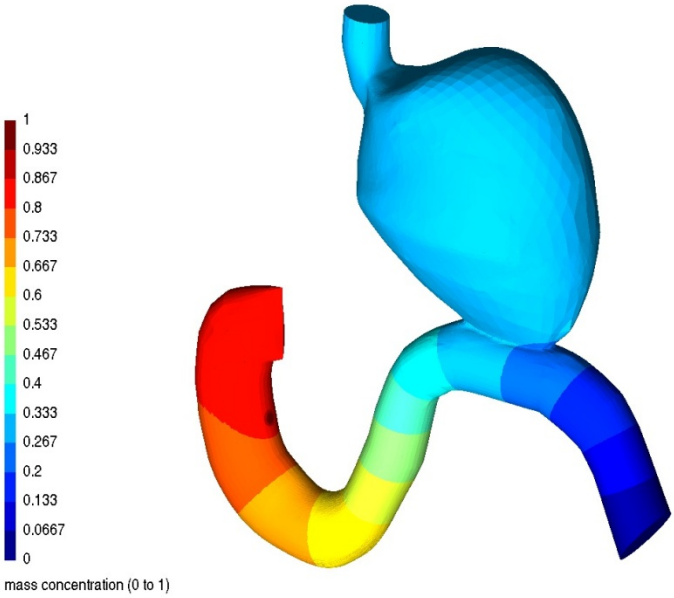

Figure 6b. Mass concentration distribution for pancreatic juice and bile - CASE B

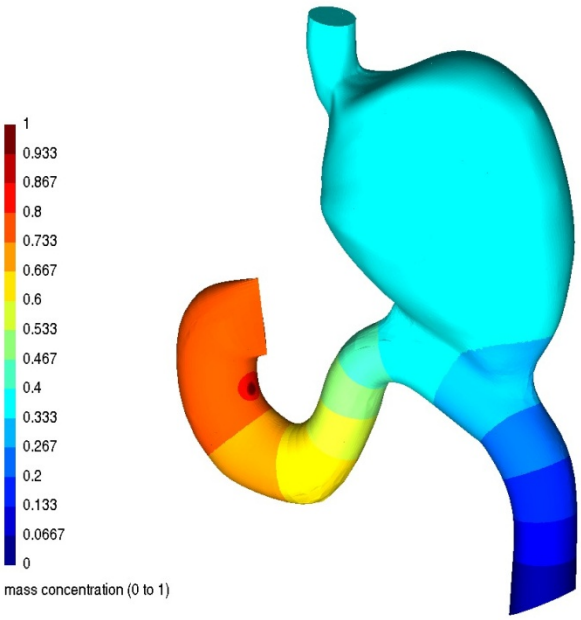

Figure 6c. Mass concentration distribution for pancreatic juice and bile - CASE C

4. Conclusion

By changing input parameters of our interactive computational model (model geometry, fluid parameters), we can improve prediction of the potential in vivo events. Also, it is possible to obtain insight into possible outcomes of different types of surgical reconstruction of the digestive tract after operations on the gastroduodenal region. This may include variations of the same surgical intervention, related to surgeons' ability or the specific anatomy of a single patient.
The practical aim of this study was to provide an insight into the physical conditions within the duodenal stump after gastric resection, in relation to the pathogenesis of duodenal stump blowout, and the implications for the surgical technique itself. Our comprehensive computational models include duodenal pressure quantification, which causes disruption of the duodenal stump closure. Such models determine shear stress and pressure distribution at the inner surface of the duodenal stump.
Our aim is to create software with DICOM images, which will be able after simulation and virtual surgical intervention to suggest optimal, preferable, patient specific geometry of reconstructed gastrointestinal tract with minimal possibility of anastomosis dehiscence or duodenal stump disruption
In future, sophisticated models could establish a correlation between variations of geometry after surgical reconstruction, duodenal tissue quality, duodenal flow, intraluminal pressure distribution, in order to quantify pathological conditions and critical levels of increased intraluminal duodenal pressure, leading to dehiscence and consecutive life treating postoperative complication.

Acknowledgement

This work was supported in part by Ministry of Science in Serbia, Grant ON174028 and III41007.

References

1. Scott DJ,Cendan JC, Pugh CM, Minter RM, Dunnington GL, Kozar RA.The changing face of surgical education: simulation as the new paradigm.J Surg Res. 2008; 15; 147(2): 189–193. PMCID: PMC2676783 doi: 10.1016/j.jss.2008.02.014.
2. Toro C, Robiony M, Costa F, Zerman N, Politi M. Feasibility of preoperative planning using anatomical facsimile models for mandibular reconstruction. Head Face Med. 2007; 3: 5. doi: 10.1186/1746-160X-3-5. PMCID: PMC1783647
3. Crooijmans HJA, Laumen AMRP, van Pul C, van Mourik JBA. A New Digital Preoperative Planning Method for Total Hip Arthroplasties.ClinOrthopRelat Res. 2009; 467(4): 909–916. doi:10.1007/s11999-008-0486-y. PMCID: PMC2650039
4. Edelbroek M, Horowitz M, Dent J, Sun WM, Malbert C, Smout A, Akkermans L. Effects of duodenal distention on fasting and postprandial antropyloroduodenal motility in humans. Gastroenterology. 1994;**106**:583–592.

5. Rao SS, Lu C, Schulze-Delrieu K. Duodenum as a immediate brake to gastric outflow: a videofluoroscopic and manometric assessment. Gastroenterology. 1996;**110**:740–747.
6. Andrews JM, Doran SM, Hebbard GS, Malbert CH, Horowitz M, Dent J. Nutrient-induced spatial patterning of human duodenal motor function. Am J PhysiolGastrointest Liver Physiol. 2001;**280**:501–509.
7. Lingenfelser T, Sun W, Hebbard GS, Dent J, Horowitz M. Effects of duodenal distension on antropyloroduodenal pressures and perception are modified by hyperglycemia. Am J Physiol. 1999;**276**:711–718.
8. Horowitz M, Dent J, Fraser R, Sun W, Hebbard G. Role and integration of mechanisms controlling gastric emptying. Dig Dis Sci. 1994;**39**:7–13.
9. Guyton AC, Hall JE. Textbook of Medical Physiology. 11th ed. Elsevier Inc: Philadelphia; 2006. pp. 784–788.
10. Lammers WJ, Slack JR. Of slow waves and spike patches. News Physiol Sci. 2001;**16**:138–144.
11. Feinle C, D'Amato M, Read NW. Cholecystokinin-A receptors modulate gastric sensory and motor responses to gastric distension and duodenal lipid. Gastroenterology. 1996;**110**:1379–1385.
12. Schaap HM, Smout AJ, Akkermans LM. Myoelectrical activity of the Billroth II gastric remnant. Gut. 1990;**31**:984–988.
13. Hai-Tao Wang, Qi-Cheng Lu, Qing Wang, Rong-Chao Wang, Yun Zhang, Hai-Long Chen, Hong Zhao, and Hai-XinQian. Role of the duodenum in regulation of plasma ghrelin levels and body mass index after subtotal gastrectomy. World J Gastroenterol. 2008 April 21; 14(15): 2425–2429. doi: 10.3748/wjg.14.2425. PMCID: PMC2705102
14. Imam H, Sanmiguel C, Larive B, Bhat Y, Soffer E. Study of intestinal flow by combined videofluoroscopy, manometry, and multiple intraluminal impedance. Am J PhysiolGastrointest Liver Physiol. 2004;**286**:263–270.
15. Faas H, Hebbard GS, Feinle C, Kunz P, Brasseur JG, Indireshkumar K, Dent J, Boesiger P, Thumshirn M, Fried M, et al. Pressure-geometry relationship in the antroduodenal region in humans. Am J PhysiolGastrointest Liver Physiol. 2001;**281**:1214–1220.
16. Nguyen HN, Silny J, Wuller S, Marschall HU, Rau G, Matern S. Chyme transport patterns in human duodenum, determined by multiple intraluminal impedancometry. Am J Physiol. 1995;**268**:700–708.
17. Meeroff JC, Go VL, Phillips SF. Control of gastric emptying by osmolality of duodenal contents in man. Gastroenterology. 1975;**68**:1144–1151.
18. Shirazi S, Schulze-Delrieu K, Brown CK. Duodenal resistance to the emptying of various solutions from the isolated cat stomach. J Lab Clin Med. 1988;**111**:654–660.
19. Degen LP, Beglinger C. Postoperative gastrointestinal physiology following operations on the stomach. Pancreatology. 2001;**1suppl 1**:9–13.
20. Schwarz A, Buchler M, Usinger K, Rieger H, Glasbrenner B, Friess H, Kunz R, Beger HG. Importance of the duodenal passage and pouch volume after total gastrectomy and reconstruction with the Ulm pouch: prospective randomized clinical study. World J Surg. 1996;**20**:60–66.
21. Tatishvili GG, Beriashvili ZA. [Prevention of duodenal hypertension after gastrectomy]. VestnKhirIm I IGrek. 1990;**144**:24–27.

22. Lee KD, Liu TW, Wu CW, Tiu CM, Liu JM, Chung TR, Chang JY, Whang-Peng J, Chen LT. Non-surgical treatment for afferent loop syndrome in recurrent gastric cancer complicated by peritoneal carcinomatosis: percutaneous transhepatic duodenal drainage followed by 24-hour infusion of high-dose fluorouracil and leucovorin. Ann Oncol. 2002;**13**:1151–1155.
23. Kim HC, Han JK, Kim KW, Kim YH, Yang HK, Kim SH, Won HJ, Lee KH, Choi BI. Afferent loop obstruction after gastric cancer surgery: helical CT findings. Abdom Imaging. 2003;**28**:624–630.
24. Schwartz S. Principles of Surgery. In: S Ashley., editor. Stomach: Surgery of the Stomach. 7 th ed. McGraw-Hill: New York; 1998. pp. 163–164.
25. Eagon JC, Miedema BW, Kelly KA. Postgastrectomy syndromes. SurgClin North Am. 1992;**72**:445–465.
26. Ponsky TA, Brody F, Pucci E. Alterations in gastrointestinal physiology after Roux-en-Y gastric bypass. J Am Coll Surg. 2005;**201**:125–131.
27. Pedrazzani C, Marrelli D, Rampone B, De Stefano A, Corso G, Fotia G, Pinto E, Roviello F. Postoperative complications and functional results after subtotal gastrectomy with Billroth II reconstruction for primary gastric cancer. Dig Dis Sci. 2007;**52**:1757–1763.
28. Yasuda K, Shiraishi N, Adachi Y, Inomata M, Sato K, Kitano S. Risk factors for complications following resection of large gastric cancer. Br J Surg. 2001;**88**:873–877.
29. Tsuei BJ, Schwartz RW. Management of the difficult duodenum. Curr Surg. 2004;**61**:166–171.
30. Kojic M., Filipovic N., Stojanovic B., Kojic N., Computer Modeling in Bioengineering: Theoretical Background, Examples and Software. John Wiley and Sons, Chichester, England, 2008.
31. Filipovic, N., A. Cvetkovic, V. Isailovic, Z. Matovic, M. Rosic and M. Kojic, Computer simulation of flow and mixing at the duodenal stump after gastric resection, *World Journal of Gastroentrology*, 2009, **15** (16), 1990-1998.
32. Olah A, Belagyi T, Neuberger G, Gamal EM. Use of different absorbable sutures for continuous single-layer anastomosis in the gastrointestinal tract. A prospective, randomized study. Dig Surg. 2000;**17**:483–485.
33. Weil PH, Scherz H. Comparison of stapled and hand-sutured gastrectomies. Arch Surg. 1981;**116**:14–16.

MODELING OF DIFFUSION WITHIN NANOCHANNELS WITH SURFACE EFFECTS

M. Milosevic[1], A.Ziemus[2], M.Ferrari[2], M.Kojic[1,2]

[1] Bioengineering Research and Development Center, BioIRC, Kragujevac
Prvoslava Stojanovica 6, 34000 Kragujevac
e-mail: miljan.m@kg.ac.rs
[2] The Methodist Hospital Research Institute, Houston, USA,
aziemus@tmhs.org; mferrari@tmhs.org; mkojic@tmhs.org

Abstract. Successful hierarchical modeling approach which accounts for interface effects on diffusivity is presented in this work. A Molecular Dynamics derived diffusivity scaling scheme is incorporated into a Finite Element Method to model transport through a nanochannel. Comparison with experiments through a nanofluidic membrane showed interface effects to be important. We show robustness of our continuum model in addressing complex diffusion phenomena in biomedical and engineering applications by providing a hierarchical coupling of molecular scale effects and preserving computational Finite Element Method speed.

1. Introduction

Recent technological advances enabled using nanoscale dimensions, opening reproducible fabrication of nanofluidic devices with characteristic size from several hundred down to few nanometers [1]. Emerging new material properties and transport phenomena make nanofluidic devices appealing for novel biomedical and industrial applications, including drug delivery [2], where precise mass exchange and timing are essential. Accurate prediction of the diffusive transport is needed for rational design of nanofluidic components and control of physical phenomena.

Modeling of diffusive transport in different size channels was approached by many studies, revealing that diffusivity, or diffusion coefficient, of molecules becomes sensitive to proximity to a solid surface [3]. Our recent molecular dynamics study suggested that molecular diffusivity is a function of a non-linear coupling of confinement and concentration effects. The same study showed that molecular diffusivity is reduced non-linearly to negligible values when approaching solid interface. In these conditions new transport regimes, such as saturated and concentration-dependent, may be established [4]. Analysis of those transport regimes requires novel tools, capable of integrating molecular scale information into complex macroscale models of nanofluidic devices.

Although molecular dynamics can be a powerful tool to address physics, modeling the diffusive transport through a whole device is far beyond today practical use. Various sophisticated methods which employ the continuum approach were developed to treat porous systems accounting for their thermodynamic characteristics, but still leaving interface physics aside. The most developed continuum discretization methods is the Finite Element Method (FEM) which offers computational robustness and flexibility for the analysis of transport in any device architecture and with a time-scale commonly many orders of magnitude larger than in case of MD. FEM can also be used to model nanofluidic elements with coupling MD and FEM into hybrid methods [5].

However, the FEM relies on the continuum approach, which does not incorporate interface effects and would fail to predict diffusive transport accurately. To challenge that, we approached this problem by introducing interface and concentration effects to diffusivity by a hierarchical approach. We first studied the diffusion within a nanochannel in general and then validated it by comparing computed and experimental results of glucose release through nanochanneled membranes.

2. Basic Equations

2.1. Diffusion

Classical continuum theories of diffusion through homogenous media are based on Fick's law:

$$\boldsymbol{J} = -D\nabla c \,. \tag{1}$$

where $\boldsymbol{J}$ is the mass flux along the concentration gradient ∇c, with diffusion coefficient (diffusivity) D. In reality, many experiments deal with non-ideal solutions, where D depends on concentration, i.e. D=D(c). In a nanoconfinement, the ratio of diffusion phase volume to the area of the interface is small, and interface affected domain may occupy a substantial portion of the overall diffusion space. Therefore in addition to concentration effects, nanoconfinement complicates diffusion description by violating the continuity and homogeneity of diffusion environment, so that diffusion transport predictions according to Eq.1 may become inaccurate.

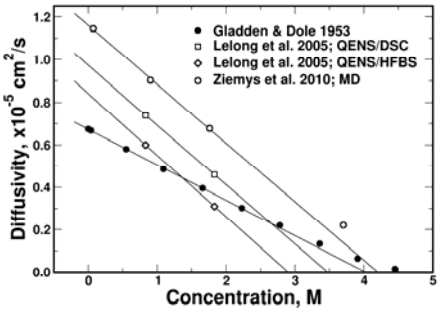

Figure 1. Linearly interpolated dependence of diffusion coefficient on concentration (according to [1]).

Experimental studies showed that D for glucose depends on concentration. Several experimental data sets for glucose diffusivity at room temperature, together with MD computed values, are plotted in Fig. 1. Data were linearly fitted within the 0-2.5 M range. Extrapolation to infinite dilution predicts D in a range from $0.7\cdot10^{-5}$ cm^2/s to $1.0\cdot10^{-5}$ cm^2/s, while handbooks suggest an approximate value of $0.6\cdot10^{-5}$ cm^2/s. The differences of the slopes and absolute values indicate that the results are sensitive to experimental conditions. For our study we have chosen the glucose D according to the largest data set of Gladden

and Dole [6] that spans over a wide range of concentrations, from 0 to 3.36 M; also that data has a D value closest to handbooks at infinite dilution.
Here we give specifics related to use of the variable diffusion coefficient obtained by MD simulations, with dependence of D on both concentration and distance from the wall. Schematics of the interpolation used to determine diffusion coefficient is shown in Figure. 2. Data obtained by MD are organized as tables and here are represented in a graphical form by set of curves $D(d)$ for constant concentrations $c_1, c_2, c_3 \ldots$.

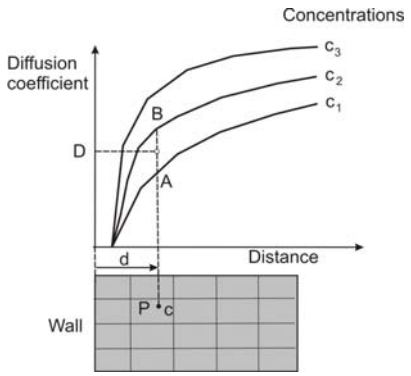

Figure 2. Schematics of the determination of diffusion coefficient from data obtained by MD. For a distance d from the wall of a material point P, diffusion coefficient $D(d,c)$ is interpolated between points A and B on two adjacent curves (for $c_1 \le c \le c_2$).

2.2 FE model

In developing the FE model we consider unsteady diffusion with the diffusion coefficient dependent on both concentration and spatial position of the point within the FE model. FE solution procedures for solving nonlinear diffusion problems have been well established and successfully used in various applications (e.g. [9], [10],[12]). The basic mass balance equation is given as:

$$-\frac{\partial c}{\partial t}+\frac{\partial}{\partial x_i}\left(D\frac{\partial c}{\partial x_i}\right)+q=0\,. \tag{2}$$

where $c\left(x_i,t\right)$ is concentration; D is the diffusion coefficients, dependent in general on the coordinates x_i and on c ; $q\left(x_i,t\right)$ is a source term; and summation over the repeated index is implied (i=1,2,3). By using a standard Galerkin procedure, this equation can be transformed into an incremental-iterative equation of balance of a finite element:

$$\left(\frac{1}{\Delta t}\mathbf{M}+{}^{n+1}\mathbf{K}^{(i-1)}\right)\Delta\mathbf{C}^{(i)}={}^{n+1}\mathbf{Q}^{S(i-1)}+{}^{n+1}\mathbf{Q}^{V(i)}-{}^{n+1}\mathbf{K}^{(i-1)}\,{}^{n+1}\mathbf{C}^{(i-1)}-\frac{1}{\Delta t}\mathbf{M}\left({}^{n+1}\mathbf{C}^{(i-1)}-{}^{n}\mathbf{C}\right)\,. \tag{3}$$

where **C** is the vector of nodal concentrations; the left upper indices n and n+1 denote values at start and end of the time step *n* of size Δt ; the indices i and i-1 correspond to the current and previous equilibrium iteration; $\mathbf{Q}^S$ and $\mathbf{Q}^V$ are surface and volumetric nodal fluxes for the element; and components of the matrices $\mathbf{M}$ and $\mathbf{K}$ are:

$$M_{IJ} = \int_V N_I N_J dV \ . \tag{4}$$

$$^{n+1}K_{IJ}^{(i-1)} = \int_V {}^{n+1}D^{(i-1)} N_{I,i} N_{J,i} dV \ . \tag{5}$$

Here N_I and N_J are interpolation functions, and $^{n+1}D^{(i-1)}$ is the diffusion coefficient corresponding to the last known concentration $^{n+1}c^{(i-1)}$ at a point within the finite element. Assemblage of equations (3) and solution procedures are performed in a usual manner and are well described in the computational mechanics literature (e.g. [9]).

3. The NDS graphical interface and FE model

In order to handle the FE model generation and postprocessing of results in an easy way, we have developed a graphical interface. This NDS interface also provides a tool to be used in the NDS design and optimization.
A 3D representation of nanochannel and finite element model used in the interface are shown in Fig. 3. The input parameters also include specification of the dependence *D*(*c*) in a tabular form for diffusion within microchannels and nanochannels; time step, number of time steps; volumes of the input and output reservoirs, and initial concentrations within the NDS. The FE model includes 1D finite elements for nanochannels.

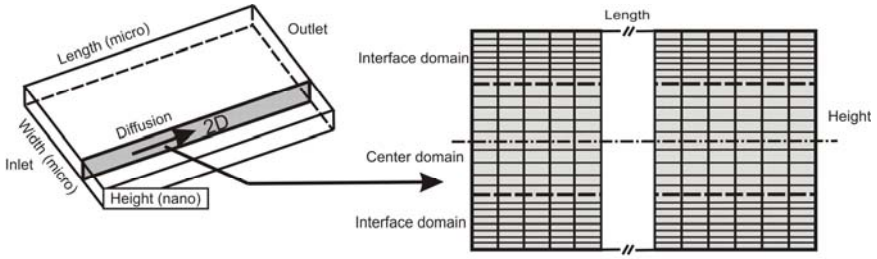

Figure 3. A 3D representation of nanochannel (left) and finite element model (right) (according to [1]).

The graphical interface provides a display of results with a number of options, such as display of concentration and mass-flux spatial distributions over time, concentration or flux evolution over time for a selected microchannel cross-section, for nanochannels, as well as mass release over selected cross-sections, nanochannels and for the entire NDS. The main menu of the interface with a generated model and concentration distribution is shown in Fig. 4.

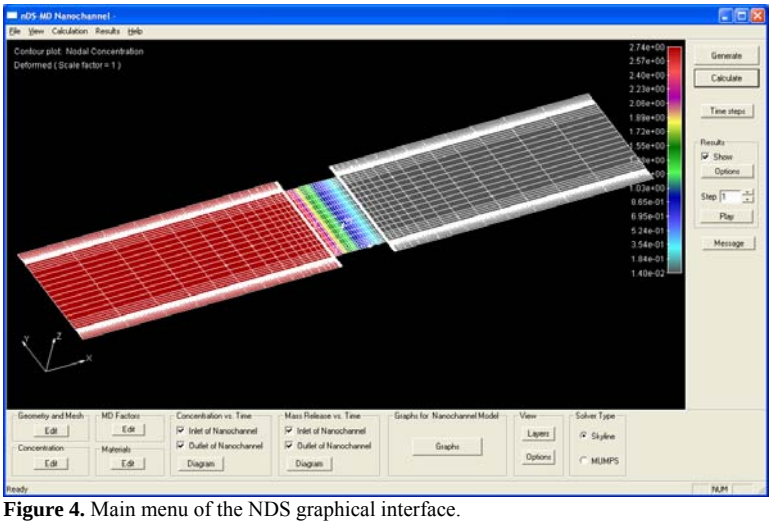

Figure 4. Main menu of the NDS graphical interface.

4. Results

First, we studied the interface effects in a simple nanochannel model as a general case. The interface effects are more pronounced in small confined spaces in which the interface domain occupies most of the volume. Therefore, we generated a 2D FE model of a nanochannel with 5 nm height and 500 nm length, where the height is comparable to thickness of the interface. A 3D schematic of the nanochannel is shown in Figure 3. Diffusion is assumed to be the same in all planes parallel to the shaded plane in the figure; hence we can use only a 2D rectangular domain bounded by nanochannel length and height. A fine mesh was used close to the nanochannel interface to better model the interface effect on the diffusivity, while a coarse mesh was employed to model the bulk of the channel where solution properties are more likely to be homogeneous. The nanochannel connects upstream and downstream reservoirs with 0.01 μl volume each. At time zero the upstream reservoir was filled with 2.75 M solution, while the other reservoir had zero concentration.
We used a representative D value for small compounds in water, where D linearly changes from $1.0 \cdot 10^{-6}$ cm^2/s at zero concentration to $0.5 \cdot 10^{-6}$ cm^2/s at 1 M. The FE calculations were performed using variable time step size, starting from very small value (0.01 s) to capture the transient diffusion regime, and then increasing it (0.5 s) for computational efficiency. We have tested three cases: D is a constant (D(const) = $1.0 \cdot 10^{-6}$ cm^2/s); D changes linearly between 0 and 2.75 M concentrations, D(c); and D is a function of concentration and the proximity to the wall, D(c,w). Results are plotted in Fig. 5B It can be seen from the calculated release profiles that the interface effects can be substantial for diffusion transport through small nanopores or nanochannels, since the D(c,w) curve differs significantly from the other two curves. On the other hand, differences between the curves D(const) and D(c) is smaller demonstrating that concentration effect is less pronounced for the 5 nm nanochannel.
We have calculated diffusive mass release in the identical system as described above, but with nanochannel heights of 10, 20 and 50 nm using D(c,w). The release profiles showed an expected faster mass release with the increase of the nanochannel height. We found that,

the interface effects on the mass release are negligible in a 50 nm nanochannel. This clearly demonstrates importance of the interface effects for diffusion through small nanochannels, or other nanoporous structures, and suggests that these effects should be taken into account in predicting diffusional mass transport through nanoporous media.

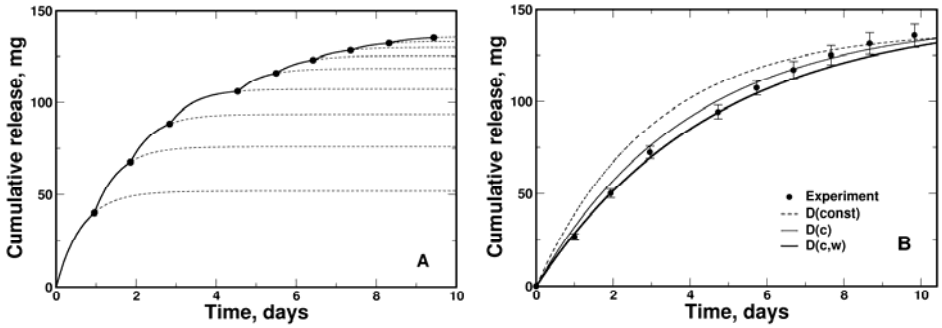

Figure 5. Predicted glucose cumulative release by FE model for a membrane with 5 nm nanochannels. ; A– a detailed picture of calculated release using D(const) (solid line – calculated release, dashed line – predicted extension of release, full circle – sampling point); B – glucose release using D=const, D dependent on concentration, and D dependent on concentration and on distance from the silicon wall .

We validated our approach by simulating experimentally tested nanofluidic systems, which displayed a non-Fickian diffusion of concentrated glucose solution through a 5 nm silicon nanochannel membrane [11]. Silicon membrane contains additional microfluidic structures with characteristic lengths of micrometers that connect upstream and downstream reservoirs. Replenishing the downstream reservoir with fresh solution during sampling times discontinuously change concentration at the outlet surface, and this also was incorporated in our calculations. The mass release experiment was further continued until the next sampling. As shown in Figure 5.A, nine sampling points are generated until glucose was depleted in upstream reservoir.

Calculated cumulative mass release curves of glucose are shown in Fig. 5.B together with experimental data. The mass release for D(const) demonstrates that Fickian diffusion (Eq. 1) has the largest deviation from the experimental data. Incorporation of concentration and interface effects reduces release rate and the mass release curves become closer to experiments. Data for correction factors for both bottom and top surface of nanochannel, according to scaling function given by Figure 1, are given in Tabels 1 and 2.

Table 1. Correction factors for top surface of nanochannel

	C1	C2	C3	C4
h-nm	0	1	2	4
0	0	0	0	0
0.5	0.00069	0.00043	0.0003	0.00042
1.5	0.00461	0.00366	0.00273	0.0028
2.5	0.00856	0.00772	0.00707	0.00673
3.5	0.00961	0.00917	0.00881	0.0085
4.5	0.00988	0.00966	0.00947	0.00927

Table 2. Correction factors for bottom surface of nanochannel

	C1	C2	C3	C4
h-nm	0	1	2	4
0.0	0.0	0.0	0.0	0.0
0.5	0.069	0.043	0.03	0.042
1.5	0.461	0.366	0.273	0.28
2.5	0.856	0.772	0.707	0.673
3.5	0.961	0.917	0.881	0.85
4.5	0.988	0.966	0.947	0.927
5.5	0.997	0.988	0.979	0.967
6.5	0.999	0.996	0.992	0.987
7.5	1	0.999	0.997	0.994
8.5	1	1	0.999	0.998
9.5	1	1	1	1
1	1	1	1	1

Diagrams of predicted change of concentration in both upstream and downstream reservoirs is given in Figure 6.A. It can be seen from Figure 6.A that concentration in both reservoirs at the end of FE simulation will be 1.37 M. Predicted glucose cumulative release by full FE model for a membrane with 5 nm nanochannel and with using different correction factors for upper and bottom wall of nanochannel is given in Figure 6.B. Results of FE modeling for Unit Mass flux in X direction for case of using different correction factors for upper and bottom surface of nanochannel is given in Figure 7.

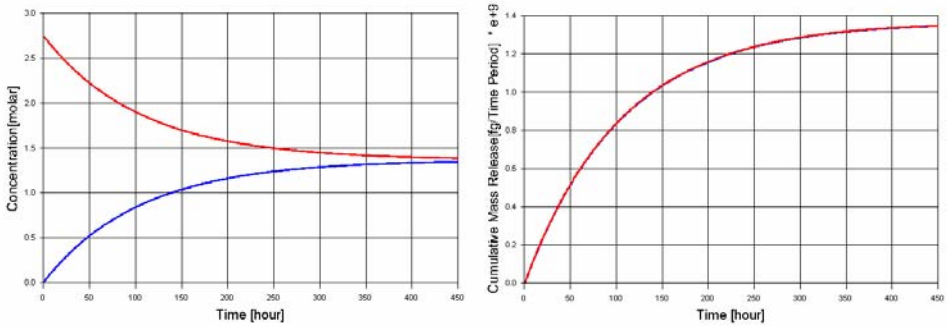

A B

Figure 6. A – predicted concentration change by FE model in nanochannel at two cross-sections: inlet (red) and outlet of nanochannel (blue). B - Predicted glucose cumulative release by FE model for a membrane with 5 nm nanochannel.

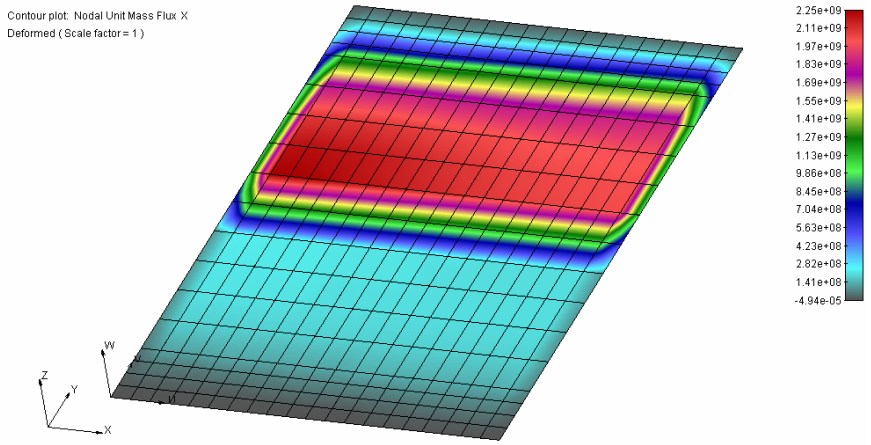

Figure 7. Results of FE computation for Unit Mass flux in X direction for case of using different correction factors for upper and down surface of nanochannel

6. Conclusions

In diffusion at the nanoscale, a complex environment is present with specific physical phenomena at the boundaries. Translational diffusivities are reduced in the fluid adjacent to the wall, which affects the overall diffusive mass transport in solutions. Therefore, the continuum based description of diffusion is inappropriate for nanoconfinement. We here present an approach to hierarchically incorporate interface effects, evaluated at the molecular level by using MD simulations, into continuum-based FE models. We introduced diffusivity scaling functions to account the proximity to the solid surface. These functions also depend on the nature of the fluid, solid, and diffusing molecules. This straightforward multiscale approach bridges molecular scale information into FE analysis without loosing the robustness of the continuum method, and offers flexibility to integrate molecular level phenomena into FE analysis.

Application of our approach showed improved prediction of diffusion through silicon nanochannels, and demonstrated that constant diffusion coefficients, or even concentration dependent diffusivities, cannot alone offer good prediction because the interface effects are important due to nanoconfinement.

Our hierarchical approach is applicable to the prediction of diffusional transport through nonoporous materials in engineering and biomedicine, and it is especially relevant for biomedical applications, as many new technologies rely on nanoscale features (nanopores, nanochannels, nanoparticles) for controlled drug delivery.

Acknowledgement

This project has been supported with federal funds from NASA under the contracts NNJ06HE06A and NNX08AW91G, Department of Defense under the contract DODW81XWH-09-1-0212, as well as funds from State of Texas Emerging Technology Fund, Nano Medical Systems (NMS), Alliance of NanoHealth (ANH), and University of Texas at Houston. The authors acknowledge the Texas Advanced Computing Center

(TACC) at The University of Texas at Austin for providing HPC resources that have contributed to the research results reported here.

The authors acknowledge the Ministry of Science of Serbia for support through Grants ON174028 and III41007.

References

[1] A. Ziemys, M. Kojic, M. Milosevic, N. Kojic, F. Hussain, M. Ferrari, A. Gratoni, Hierarchical modeling of diffusive transport through nanochannels by coupling molecular dynamics with finite element method. Journal of Computational Physics. 230(2011) 5722-5731.
[2] A. Grattoni, D. Fine, A. Ziemys, J. Gill, E. Zabre, R. Goodall,M. Ferrari, Nanochannel Systems for Personalized Therapy and Laboratory Diagnostics. Current Pharmaceutical Biotechnology. 11(4) (2010) 343-365.
[3] A. Ziemys, A. Grattoni, D. Fine, F. Hussain,M. Ferrari, Confinement Effects on Monosaccharide Transport in Nanochannels. The Journal of Physical Chemistry B. (2010) 132-137.
[4] A. Grattoni, H. Shen, D. Fine, A. Ziemys, J. Gill, L. Hudson, S. Hosali, R. Goodall, X. Liu,M. Ferrari, Nanochannel Technology for Constant Delivery of Chemotherapeutics: Beyond Metronomic Administration. Pharmaceutical Research. (2010) 1-9.
[5] R. Rudd,J. Broughton, Coarse-grained molecular dynamics and the atomic limit of finite elements. Physical Review B. 58(10) (1998) 5893-5896.
[6] J.K. Gladden,M. Dole, Diffusion in supersaturated solution-II: glucose solutions. J. Am. Chem. Soc. 75 (1953) 3900-3904.
[7] Kojic M, Filipovic N, Stojanovic B, Kojic N (2008) *Computer Modeling in Bioengineering – Theoretical Background, Examples and Software*, J Wiley and Sons, Chichester, England.
[8] Kojic M and Bathe K J (2005) Inelastic Analysis of Solids and Structures, Springer, Berlin-Heildelberg, Germany.
[9] K. Bathe, *Finite element procedures*. 1996, Englewood Cliffs, New Jersey: Prentice-Hall.
[10] T. Hughes, *The finite element method: linear static and dynamic finite element analysis*. 2000, New York: Dover Publications.
[11] D. Fine, A. Grattoni, S. Hosali, A. Ziemys, E. De Rosa, J. Gill, R. Medema, L. Hudson, M. Kojic,M. Milosevic, A robust nanofluidic membrane with tunable zero-order release for implantable dose specific drug delivery. Lab on a Chip. (2010).
[12] N. Kojic, A. Kojic,M. Kojic, Numerical determination of the solvent diffusion coefficient in a concentrated polymer solution. Communications in Numerical Methods in Engineering. 22(9) (2006) 1003-1013.

ARTOOL: A PLATFORM FOR THE DEVELOPMENT OF MULTI-LEVEL PATIENT-SPECIFIC ARTERY AND ATHEROGENESIS MODELS

Z. Milosevic[1,2], B. Stojanovic[3], V. Isailovic[1], D. Nikolic[3], D. Milasinovic[1,3], M. Radovic[1,2], T. Exarchos[4], K. Stefanou[4], P. Siogkas[4], A. Sakelarios[4], D. Fotiadis[4], O. Parodi[5], N. Zdravkovic[6], M. Kojic[1,7] and N. Filipovic[1,2]

[1] Bioengineering Research and Development Center, BioIRC Kragujevac
Prvoslava Stojanovica 6, 34000 Kragujevac
e-mail: mradovic@kg.ac.rs, racanac@kg.ac.rs
[2] Faculty of Mechanical Engineering, University of Kragujevac
Sestre Janjic 6, 34000 Kragujevac
e-mail: fica@kg.ac.rs
[3] Faculty of Natural Science, University of Kragujevac
Radoja Domanovića 12, 34000 Kragujevac
e-mail: bobi@kg.ac.rs
[4] Foundation of Research and Technology Hellas -Biomedical Research Institute, Ioannina, Greece and with the Unit of Medical Technology and Intelligent Information Systems, Dept of Material Science and Engineering, University of Ioannina, Ioannina, Greece.
(email: exarchos@cc.uoi.gr)
[5]Instituto di Fisiologia Clinica, Consiglio Nazionale delle Ricerche, Pisa, Italy
(email: oberpar@tin.it)
[6]Medical Faculty, University of Kragujevac
e-mail: nzdravkovic@gmail.com
[7]Methodist Hospital Research Institute, Houston, USA
e-mail: mkojic@hsph.harvard.edu

Abstract – This work describes software, named ARTool, for 3D reconstruction, from different image modalities, and modeling a biological and biomechanical processes during formation and development of the atheroma. For visualization of atherosclerosis lesion, Intravascular Ultrasound (IVUS) and Angiography, Computed Tomography (CT), and Magnetic Resonance Imaging (MRI) are used. Generated medical images are processed via ARTool generating patient – specific 3D models. Arterial models are used to study blood flow dynamics, fluid solid interaction and plaque progression. ARTool is able to run all simulations simultaneously and perform the required calculations in a parallel processing mode. All data are stored and management on advanced storage and database system special developed for these purposes.

Keywords - Blood flow, 3D reconstruction, solid-fluid interaction, IVUS, MRI, CT, plaque progression, atherosclerosis.

1. Introduction

Atherosclerosis is very common cardiovascular disease and it is main cause of the death of a large amount of people every year. It is commonly referred to as a hardening or furring of the arteries because of the accumulation of lipids in the arterial wall. The transport process of atherogenic species starts with low density lipoprotein (LDL) from the bulk blood flow which contributes to lipid accumulation and formation of several plaque types. Plaque

formation is influenced by the biological, mechanical and biochemical processes. A few mathematical models have been developed in order to simulate mass transport in the large arteries and lipid accumulation in the wall. These models use Navier-Stokes equations to model bulk blood flow in the lumen, Darcy`s law to model the transmural flow in the wall of the blood vessel, convection-diffusion equations to model mass balance in the lumen and the convection-diffusion reaction equation to model mass balance in the intima and adventitia, which represents the wall. For coupling the fluid dynamics in the lumen and solute dynamics in the endothelium Kedem-Katchalsky equations were employed [1].
Computational models which are used for modeling the blood vessel flow and plaque formation are wall-free and single-layered model depending on the treatment of the arterial wall [2]. Wall free models are the simplest and are used for modeling solute dynamic in the lumen. That model treats the wall only as the boundary condition and modeling of transport processes within the wall is not possible. Unlike wall-free, single-layered models treats arterial wall as one layer of porous medium with homogenous transport properties.
In this paper we presented software ARTool. It consists of advanced tools for 3D reconstruction of arteries from different image modalities, finite element models generation, simulation tools, and post processing and visualizing tools. ARTool actually embeds a variety of 3D reconstruction algorithms from IVUS and Angiography, MRI and CT[3-5], finite element calculation and mesh generation [6]. It is capable for performing blood flow, fluid solid interaction and plaque progression simulations within the large arteries. Also it consists storage and database management system for all patient specific data. The proposed tool enables clinician to perform different simulation types and predict regions prone to plaque development.

2. Methods

ARTool is capable to produce a patient specific artery and atherogenesis models by using geometry reconstructed from three different image modalities (IVUS, MRI and CT). Reconstructed geometry is further used by the IVUS [7] and MRI-CT [8] preprocessing modalities for generating three types of finite element meshes for blood flow, fluid solid interaction and plaque progression simulation. The finite element solvers, which are based on advanced finite element procedures, are adapted for specific problems considered here [9]. In the last phase the results produced by the solvers are post processed by using the visualization tool (Fig. 1).

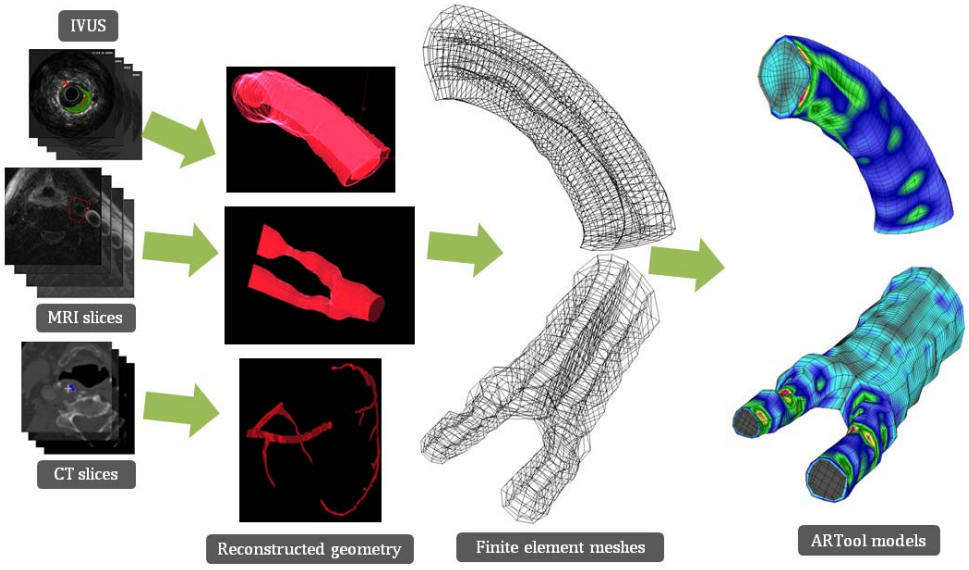

Figure 1. ARTool conceptual architecture

Every preprocessing modality has four main methods:

- Finite element (FE) mesh generation from reconstructed geometry
- Constraining mesh nodes
- Prescribing loads
- Exporting model for the solver

Highly optimized and complex algorithms are employed for generating all necessary FE mesh entities such as nodes, edges, faces, elements etc. Mesh constraining depends on the type of the simulation that will be performed. For the blood flow simulation models wall is treated as rigid and all the nodes that represents the wall are fully constrained. These models are so called wall-free models [1] (Fig 2a). Prescribing loads is also totally dependent on the type of the simulation. For the blood flow simulations in adding load phase only initial velocities are prescribed at the mesh nodes that represent the artery inlet. The last step is exporting FE mesh in textual file suitable formatted for the blood flow solver. For the fluid-solid interaction models wall and lumen are treated as the separate FE mesh. From aspect of constrains FE mesh that represents lumen is constrained in the same way as the blood flow FE mesh. The wall nodes that represent inlet and outlet are totally constrained from the displacements. All the other nodes remain unconstrained. Prescribing loads is identical as for the blood flow models. The lumen and wall FE mesh are exported into two separate files.

Modeling plaque propagation is achieved by using so called single-layered model [1] where the lumen and the wall are part of the same FE mesh but they are recognized as different entities (Fig. 2b). Constraining phase uses a few mesh nodes groups. The inlet wall and lumen nodes, nodes representing artery lumen, artery endothelium, wall nodes and shell nodes. All those groups are constrained in the appropriate way in order to simulate behavior

in the realistic conditions. In prescribing loads phase besides the prescribing velocities at the lumen inlet, the prescribing fluxes at specific elements and the prescribing concentrations are necessary in order to simulate plaque propagation processes. In that way FE mesh is exported in one input file.

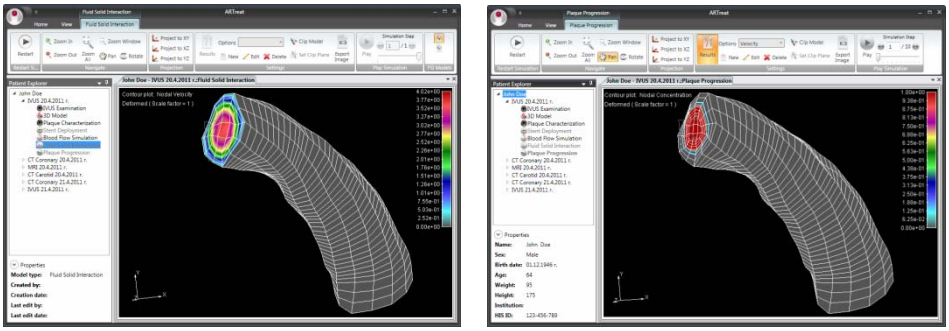

a. Wall-free model b. Single-layered model

Figure 2. ARTool – Blood flow simulation (a), and plaque propagation simulation (b)

In the last phase, after running simulations using solvers, the collected results can be presented by sophisticated post processing software which can visualize a huge amount of the mesh entities and to manipulate them simultaneously. Any user can choose which results will be shown, change view of the model by rotating, panning and sectioning the model with the clip plane option (Fig. 3).

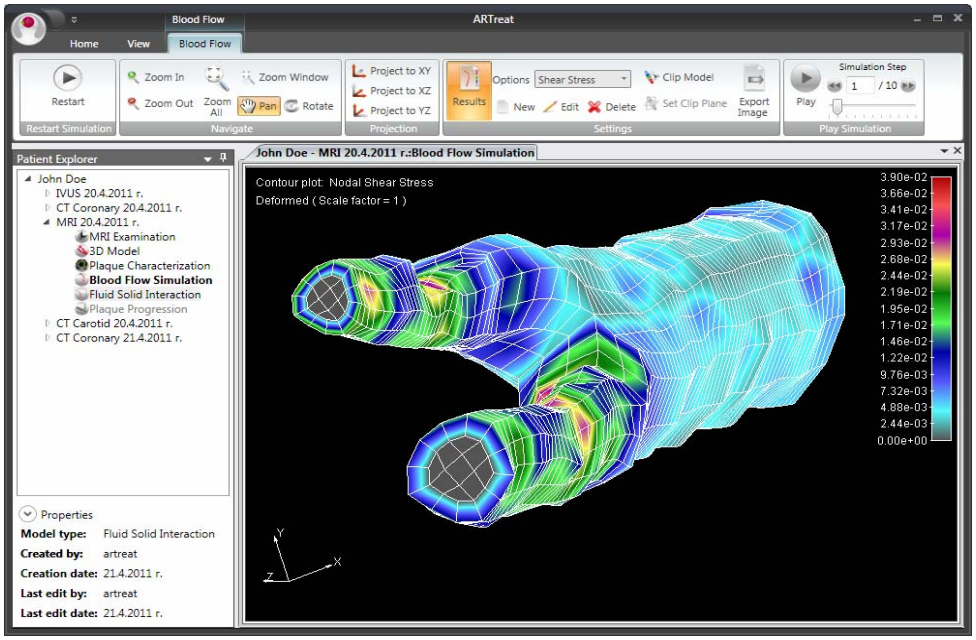

Figure 3. ARTool: MRI module - Blood flow simulation – Shear stress distribution

Different result for different simulation types may be presented (Fig. 3). Blood flow simulations provides velocity, pressure and shear stress distribution. Solid-fluid interaction simulation, in advance, provides also displacement field. Plaque propagation simulation provides, besides other results, LDL, Cytokines, Macrophage, and Wall LDL distributions.
The ARTool software architecture is based on the Window Presentation Foundation technology, using the Windows Communication Foundation services approach (Fig. 4). The software pattern used for this approach is the Model-View-Presenter Design Pattern. This Model-view-presenter (MVP) is a user interface design pattern engineered to facilitate automated unit testing and improve the separation of concerns in the presentation logic. The *model* is an interface defining the data to be displayed or otherwise acted upon in the user interface. The *view* is an interface that displays data (the model) and routes user commands (events) to the presenter to act upon that data. The *presenter* acts upon the model and the view. It retrieves data from repositories (the model) and persists, and further formats it for display in the view.

ARTool uses MVP design pattern as follows:

- The Model contains the data objects of the ARTool software.
- The View is a user control which contains windows components (like text boxes and buttons). The view raises events during interaction with the viewer.
- The Presenter deals with communication with the View and handles the events raised by the View, in terms of software engineering layers.

In terms of software engineering layers ARTool employes the following approach:

- The Data Storage Layer contains the ARTool database and the configuration files needed for the software operation.
- The Data Access Layer contains the implementation of the data retrieval and data storage methods from/to the database and files, respectively.
- The Business Logic layer contains the implementation of the core methods as services and actual data context.
- The Graphical User Interface Layer contains all the graphical user controls (Views), which can be used in Presentation Layer.

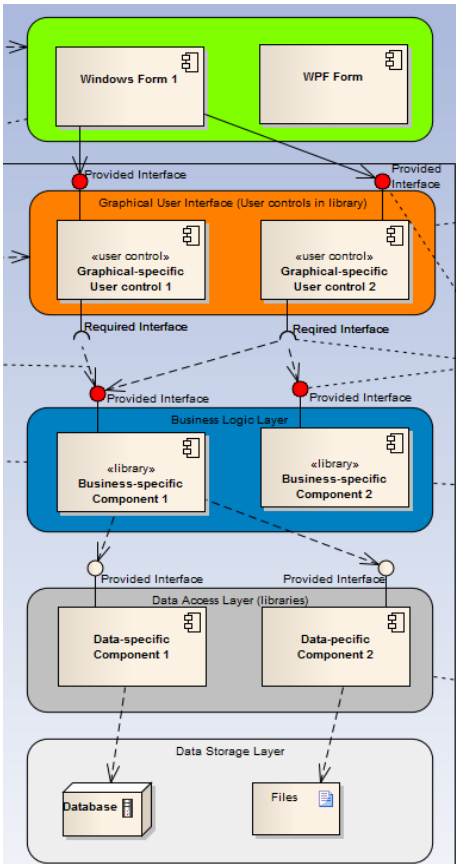

Figure 4. Architecture of the ARTool platform

In all of the above, the layers communicate using Services, which contain implementation of the business logic methods and algorithms using the Windows Communication Foundation principles and Interfaces, which deal with the communication of the Services.

3. Results and Discussion

ARTool represents a package of tools which can be used for 3D reconstruction, visualization and prediction of the plaque development. Results obtained by the algorithms that are employed for the 3D reconstruction and modeling are compared with the results from experimental studies. This comparison gives an evaluation how precise and accurate the computed results can be when compared with experimental recordings. Advantage of the ARTool is a possibility to visualize and present spatial distribution of biomechanical quantities which is practically impossible to obtain without modeling. Hence, the ARTool represents a valuable instrument for better diagnosis of specific patient conditions related to atherosclerosis.

The ARTool provides accurate 3D artery reconstruction from various image modalities, IVUS, Angiography, MRI and CT with ability of detection of luminal narrowing, on one side, and generating finite element models and processing them, on the other side. Also, ARTool is equipped with powerful post-processing software which is able to visualize all necessary entities of simulations. Friendly user interface serves to user to operate with this software with a little effort.

With fully automated and fast processing of a 3D reconstruction and FE simulation, ARTool is capable to provide important information such as length of the arterial segment, plaque volume, minimum and the mean cross sectional area, the length of the stenosis, and the maximum plaque burden. Also, FE simulations provide data such as velocity, pressure and shear stress distribution for the blood flow, as well as wall deformation in the case when the fluid-solid interaction models are used. The plaque progression simulations provide LDL, macrophage, cytokines and foam cells distributions. Both methodologies represent a patient-specific modeling for clinical treatment decisions. Furthermore, the methodologies employ experimental recordings, while sensitivity analysis on a variety of parameters provides an estimation of parameters used in the models.

Acknowledgement

This work was supported in part by the European Commission (Project ARTREAT, ICT 224297) and Ministry of Science in Serbia, Grant ON174028 and III41007.

References

[1] Nanfeng, S., Nigel, W., Alun, H., Simon, T., X Yun, X., "Fluid-Wall Modelling of Mass Transfer in an Axisymmetric Stenosis: Effects of Shear-Dependent Transport Properties" vol. 34 2006 pp. 1119-1128.

[2] Holzapfel, G., Gasser, T., Ogden, R., "A New Constitutive Framework for Arterial Wall Mechanics and a Comparative Study of Material Models," *Journal of Elasticity*, vol. 61, 2000, pp. 1-48

[3] Bourantas, C., Kourtis, I., Plissiti, M., Fotiadis, D., Katsouras, C., Papafaklis, M., Michalis, L., "A Method for 3D reconstruction of coronary arteries using biplane angiography and intravascular ultrasound images," *Comp. Med. Imag. Gr*, vol. 29, 2005, pp. 597-606.

[4] Bourantas, C., Kalatzis, F., Papafaklis, M., Fotiadis, D., Tweddel, A., Kourtis, I., Katsouras, C., Michalis, L., "ANGIOCARE: An Automated System for Fast Three- Dimensional Coronary Reconstruction by Integrating Angiographic and Intracoronary Ultrasound Data," *Cath. and Cardio. Interv.*, vol., 72, 2008, pp. 166 – 175

[5] Zifan, A., Liatsis, P., Kantartzis, P., Gavaises, M., Karcanias, N., Katritsis, D., "Automatic 3D Reconstruction of Coronary Artery Centerlines from Monoplane X-ray Angiogram Images," *International J. of Biolog. and Med. Sciences*, vol. 1, 2008, pp. 44 – 49

[6] Filipovic, N., Meunier, N., Boynard, M., Kojic, M., Fotiadis, D., "A 3D computer simulation of plaque formation and development in coronary artery", *Proceedings of ASME 2010 First Global Congress on NanoEngineering for Medicine and Biology, NEMB2010*, February 7-10, 2010 Houston, TX, USA.

[7] Plissiti, M., Fotiadis, D., Michalis, L., Bozios, G., "An Automated Method for Lumen and Media-Adventitia Border Detection in a Sequence of IVUS Frames," *IEEE trans on Inf Tech. in Biomed,* vol.8, 2004, pp. 131-141.

[8] Milner, J., Moore, J., Rutt, B., Steinman, D., "Hemodynamics of Human Carotid Artery Bifurcations: Computational Studies with Models Reconstructed from Magnetic Resonance Imaging of Normal Subjects," *J Vasc Surg.*, 1998, vol. 28, pp. 143-56

[9] Kojic M., Filipovic N., Stojanovic B., Kojic N., *Computer Modeling in Bioengineering: Theoretical Background, Examples and Software.* John Wiley and Sons, Chichester, England, 2008.

MODELING ABLATION ON THE ENDOCARDIUM AND TEMPERATURE DISTRIBUTION DURING RF ABLATION

M. Obradovic[1,3], A. Avilla[2], A. Thiagalingam[2] and N. Filipovic[1,3]

[1] Bioengineering Research and Development Center, BioIRC Kragujevac, Serbia
Prvoslava Stojanovica 6, 34000 Kragujevac
e-mail: dmilashinovic@kg.ac.rs
[2] MGH, Harvard University, Boston, USA
55 Fruit Street, Boston, MA 02114
e-mail: andre_davila@hotmail.com
[3] Faculty of Mechanical Engineering, University of Kragujevac, Serbia
Sestre Janjic 6, 34000 Kragujevac
e-mail: fica@kg.ac.rs

Abstract. A three – dimensional finite element model for endocardial radiofrequency ablation is presented. Temperature distribution through the heart during ablation was investigated for three cases: 1) when blood flow through the coronary artery is regular, 2) when blood flow through the coronary artery is equal zero, and 3) when there is no blood in the coronary artery (air was modeled in the coronary artery). Effects of parameters, such as blood flow rate and applied power (voltage on the electrode) are investigated. It is shown that the blood flow in the coronary artery does not have significant influence on the temperature distribution. Also, temperature of range 50° – 100° C for applied constant voltage of 15V is a good choice.

1. Introduction

Radio Frequency (RF) ablation is a medical procedure used to correct irregularity in heart conduction system or to destroy tumors and other nonfunctional damaged tissue by heat [1]. RF ablation uses high frequency alternating current to remove medical irregularity. General advantage of the RF ablation, compared to using low frequency alternating current or pulses of direct current is reflected in the indirect stimulation of nerves or heart muscle; and can therefore often be used without the need for general anesthetic.

Using high frequency alternating current (generator that produces radio frequency waves) causes friction between ions which are placed in the area around electrode or between specially prepared electrodes [2]. In patient tissue cells certain "disturbance" occurs that releases heat, which is used as a destroyer of diseased tissue. The heat causes destruction of tumor cells or damaged cells, but can destroy part of healthy tissue, which is surrounding tumors, or damaged tissue. When it is used electrical knife source is a direct–electric current.

RF ablation can be applied to remove lung tumors, breast cancer, bone cancer and liver tumors, for treating varicose veins, to remove pain in lumbar spine, for treating heart arrhythmias.

Application of RF ablation on heart muscle is very important because patients can be cured from heart arrhythmias. Heart ablation can be endocardial or epicardial, depending on which side of heart muscle the electrode are positioned. Epicardial ablation can be done on pulsating or stopped heart and it is more invasive procedure than endocardial ablation, but

in spite that, it is important alternative to endocarial ablation, because it avoids direct contact with blood and therefore gives clear view of ablating area. In practice most ablations are of endocardial type.
Before ablation, electro-physiologists examine the heart and mark precisely part of the heart which causes irregular beats.
The electrode is mounted on the distal end of catheter via a vein (upper or bottom) until an endocardial location for ablation is reached (Figure 1). Usually electrode is introduced through the leg, in the area of the crotch and guides through bottom vein to the heart [3].
The possible pathways for insertion catheter to heart are shown in Figure 1.

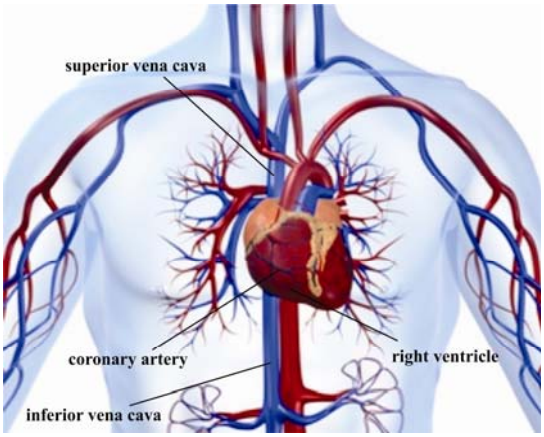

Figure 1. The paths for insertion catheter inside the heart

After electrode is positioned, which follows on the monitor by setting ultrasounds on the catheter or by taking pictures using X-rays, the electrode, which is placed on the top of catheter begins to emit radio waves (radio energy). The released energy is transformed in the heat energy to damage selected cells, so other cells, without damaging, will overtake function in conduction of the electrical impulses. Heart gets a regular electrical pathway and works properly from SA node - to AV node – to Purkinje cells pathway (Figure 2).

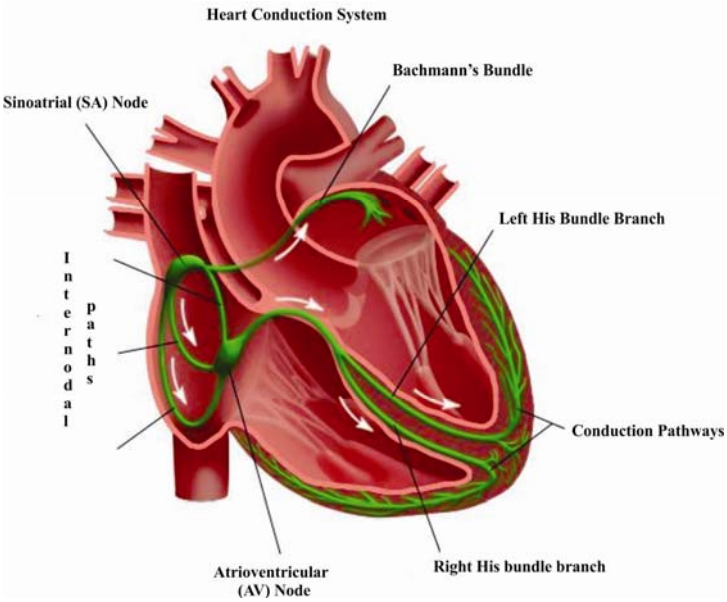

Figure 2. The paths for insertion catheter inside the heart

During the modeling process temperature field is calculated. This field is formed around electrode, in the contact point with the heart muscle. During the modeling process there are many parameters which have to be determined: dimensions of lesions (wounds, by heat affected and destroyed area), effect of blood flow on forming temperature field (either through coronary artery or heart), use of saline and its layer thickness, used voltage on electrode, contact width between electrode and heart, etc. Myocardium becomes nonviable at 50° C, which means that it is necessary to reach temperature over 50° C to destroy damaged cells, but not over 100° C, because of the patient safety.

The computational model in this study was formed using Finite Element Method (FEM). The part of endocardium on the right side of the heart, in the right chamber area is modeled (Figure 3). The model includes coronary artery with average diameter of 3mm. The three-dimensional finite element mesh of the model is shown in the Figure 4.

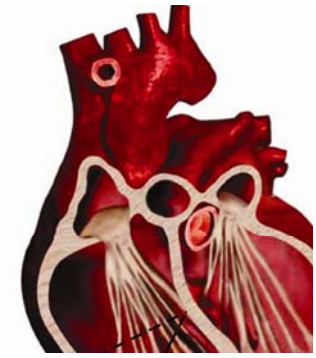

Figure 3. Chamber area used in simulation

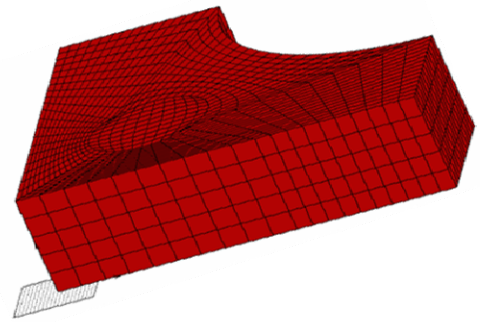

Figure 4. Finite element mesh of model

Model is formed using ***PakG*** software. Finite element mesh in XY-plate with marked characteristic points is shown in Fig. 5. The values of coordinates for characteristic points are given in Table 1. The depth in the Z-direction is 5mm. All other values are expressed in millimeters.

	x	y
A	0	10
B	4	10
C	4.242641	4.242641
D	10	4
E	10	0
F	6	0
G	0	0
H	0	6
O	3	3
M	1.93934	4.06066
N	4.06066	4.06066
R	4.06066	1.93934
S	1.93934	1.93934

Table 1 – Coordinates of characteristic points of model

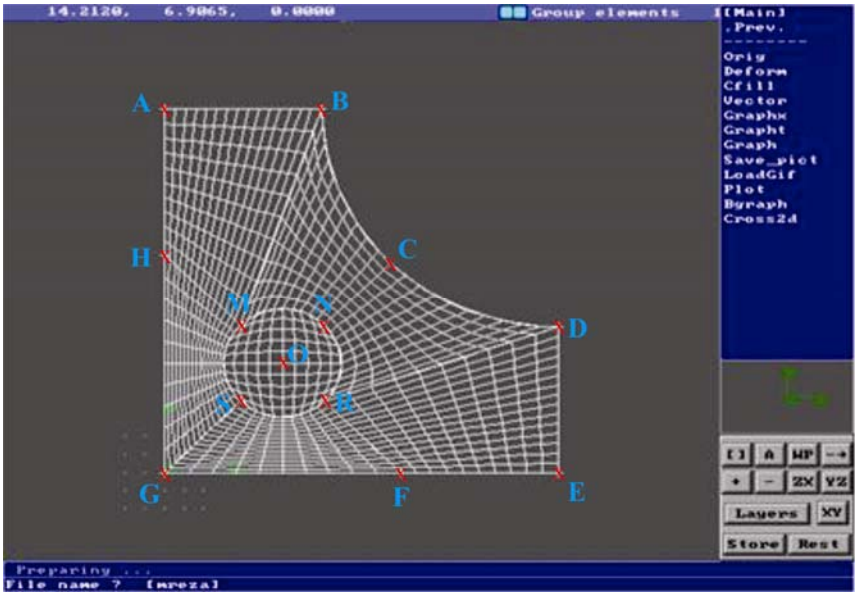

Figure 5. Model in XY-plate with characteristic points

The material characteristics for myocardium, blood and air are given in the Table 2.

	ρ (kg/mm^3)	c (J/kg/°C)	σ (S/mm)	K (W/mm/°C)	μ (kg/s/mm)
Myocardium	1.2E-06	3.2E+09	6.1E-10	7.0E+02	0.0E+00
Blood	1.064E-06	3.66E+09	9.95E-10	4.9E+02	3.0E-06
Air	1.127E-9	1.005E+09	5.0E-24	2.71E+01	1.9125E-08

Table 2 – The material properties for myocardium, blood and air

2. Methods

2.1 Governing equations

A mathematical model is based on the principles of Joule heating and approximation that electrical field generated by the electrode is quasi-static.

Joule effect. Effect of warming conductor through which electric current flows is known as effect of Joule heating.
For long cylindrical conductor with constant cross section inside the electrical field is homogenous and power can be expressed as:

$$P = RI^2 = \rho \frac{l}{S}(\vec{J}\vec{S})^2 = \rho \vec{J}^2 Sl = \rho \vec{J}^2 V = \vec{E}\vec{J}V \tag{1}$$

Volume density of power transformation of the electric energy in the thermal energy is:

$$\frac{P}{V} = \vec{J}\vec{E} = \rho J^2 = \frac{J^2}{\sigma} = \frac{\sigma^2 E^2}{\sigma} = \sigma E^2 = \sigma(-\nabla\varphi)^2 = \sigma \nabla\varphi \cdot \nabla\varphi \tag{2}$$

and represents Joule law in the local form [4]. In Equation (2) σ is the electric conduction, and J is the density of current which flows through conductor.
Temperature is function of position, space coordinates, and time and can be expressed in shape T=T(x,y,z,t).
So, according to Joule heating principle the temperature T(x,y,z,t) satisfies equation:

$$\rho c \frac{\partial T}{\partial t} = \nabla \cdot (\kappa \nabla T) + \sigma \nabla\varphi \cdot \nabla\varphi - \rho c v \cdot \nabla T \tag{3}$$

where κ is thermal conductivity, σ is electrical conductivity, c is the specific heat capacity, φ is electrical potential, v(x,y,z) is the blood velocity, and ρ is the mass density.
The first term on the right side of the Eq. (1) represents the convective part. The second term denotes the influence of applied electrode voltage on the generated temperature field. The last term in Eq. (1) represents the heat loss due to blood flow in the coronary artery.

Electric field. On the other hand, the electrode generates time-varying electric field E(x,y,z), which can be approximated as a quasistatic by $E = \nabla\varphi$, where φ must satisfy equation:

$$\nabla \cdot (\sigma \nabla\varphi) = 0 \tag{4}$$

Equation (4) represents the Laplace equation [5], [6] from which can be calculated current density and power of electric field.

Blood flow. Since simulation includes blood flow through the coronary artery it is necessary to write equation which will describe it– in this case it is Navier – Stokes equation.

2.2 Finite element modeling

In this simulation 3D mesh generation of 8-node finite element is implemented. The three – dimensional flow of a viscous incompressible fluid is governed by the Navier – Stokes equation

$$\rho\left(\frac{\partial \upsilon_i}{\partial t}+\upsilon_j\frac{\partial \upsilon_i}{\partial x_j}\right)=-\frac{\partial p}{\partial x_i}+\mu\left(\frac{\partial^2 \upsilon_i}{\partial x_j \partial x_j}+\frac{\partial^2 \upsilon_j}{\partial x_j \partial x_i}\right) \tag{5}$$

where ρ is the fluid density, υ_i is the blood velocity in x_i direction, p is the pressure, μ is the dynamic viscosity and summation is assumed on the repeated indices, i,j=1,2,3. This equation represents the balance of linear momentum.
In the analysis it is considered that the convergence is reached when the maximum absolute change in the non – dimensional velocity between the respective times in two adjacent iterations is less than 10^{-3}. A penalty formulation is used in our solver [7].
The incremental – iterative form of the equations for the current time step Δt and equilibrium iteration 'i' is

$$\begin{bmatrix} \frac{1}{\Delta t}\boldsymbol{M_v}+{}^{t+\Delta t}\boldsymbol{K_{vv}}^{(i-1)}+{}^{t+\Delta t}\boldsymbol{K_{\mu v}}^{(i-1)}+{}^{t+\Delta t}\boldsymbol{J_{vv}}^{(i-1)} & \boldsymbol{K_{vp}} & \boldsymbol{0} & \boldsymbol{0} \\ \boldsymbol{K_{vp}^T} & \boldsymbol{0} & \boldsymbol{0} & \boldsymbol{0} \\ {}^{t+\Delta t}\boldsymbol{J_{Tv}}^{(i-1)} & \boldsymbol{0} & c({}^{t+\Delta t}\boldsymbol{K_{vv}}^{(i-1)})+{}^{t+\Delta t}\boldsymbol{K_{\kappa T}}^{(i-1)} & {}^{t+\Delta t}\boldsymbol{K_{\sigma T}}^{(i-1)} \\ \boldsymbol{0} & \boldsymbol{0} & \boldsymbol{0} & {}^{t+\Delta t}\boldsymbol{K_{\sigma\varphi}}^{(i-1)} \end{bmatrix} \times \begin{Bmatrix} \Delta \boldsymbol{v}^{(i)} \\ \Delta \boldsymbol{p}^{(i)} \\ \Delta \boldsymbol{T}^{(i)} \\ \Delta \boldsymbol{\varphi}^{(i)} \end{Bmatrix} = \begin{Bmatrix} {}^{t+\Delta t}\boldsymbol{F_v}^{(i-1)} \\ {}^{t+\Delta t}\boldsymbol{Fp}^{(i-1)} \\ {}^{t+\Delta t}\boldsymbol{F_T}^{(i-1)} \\ {}^{t+\Delta t}\boldsymbol{F_\varphi}^{(i-1)} \end{Bmatrix} \tag{6}$$

Index 't+Δt' denotes that the quantities are evaluated at the end of time step. Matrix $\mathbf{M_v}$ is the mass matrix, $\mathbf{K_{vv}}$, $\mathbf{J_{vv}}$, $\mathbf{K_{\kappa T}}$ and $\mathbf{J_{Tv}}$ are the convective matrices, $\mathbf{K_{\mu v}}$ is the viscous matrix, $\mathbf{K_{\sigma T}}$ and $\mathbf{K_{\sigma\varphi}}$ are the matrices due to electrical potential, and $\mathbf{F_v}$, $\mathbf{F_p}$, $\mathbf{F_T}$, and $\mathbf{F_\varphi}$ are the force vectors. The incremental – iterative form of the equilibrium equations is [8-10]:

$$\left(\frac{1}{\Delta t}\boldsymbol{M_v}+{}^{t+\Delta t}\boldsymbol{K_{vv}}^{(i-1)}+{}^{t+\Delta t}\boldsymbol{K_{\mu v}}^{(i-1)}+{}^{t+\Delta t}\hat{\boldsymbol{K}}_{\mu v}^{(i-1)}+{}^{t+\Delta t}\boldsymbol{J_{vv}}^{(i-1)}+\boldsymbol{K_{\lambda v}}\right)\Delta \boldsymbol{v}^{(i)}={}^{t+\Delta t}\hat{\boldsymbol{F}}_v^{(i-1)} \tag{7}$$

where the matrices and vectors are:

$$
\begin{aligned}
&{}^{t+\Delta t}\hat{\boldsymbol{K}}_{\mu v}^{(i-1)} = \int_V \mu \boldsymbol{H}^T \boldsymbol{H} dV,\\
&\boldsymbol{K}_{\hat{\lambda} v} = \lambda \int_V \boldsymbol{H}^T \boldsymbol{H} dV,\\
&{}^{t+\Delta t}\hat{\boldsymbol{F}}_v^{(i-1)} = {}^{t+\Delta t}\boldsymbol{R}_B + {}^{t+\Delta t}\hat{\boldsymbol{R}}_S^{(i-1)} - \left({}^{t+\Delta t}\boldsymbol{K}_{vv}^{(i-1)} + {}^{t+\Delta t}\boldsymbol{K}_{\mu v}^{(i-1)} + {}^{t+\Delta t}\hat{\boldsymbol{K}}_{\mu v}^{(i-1)} + \boldsymbol{K}_{\hat{\lambda} v}\right) {}^{t+\Delta t}\boldsymbol{v}^{(i-1)},\\
&{}^{t+\Delta t}\left(\hat{\boldsymbol{R}}_S\right)_{i\alpha}^{(i-1)} = \int_S \boldsymbol{H}^T \left[\lambda\, {}^{t+\Delta t}\nabla \boldsymbol{v}^{(i-1)} \cdot \boldsymbol{n} + \left({}^{t+\Delta t}\nabla \boldsymbol{v}^{(i-1)} + {}^{t+\Delta t}\nabla^T \boldsymbol{v}^{(i-1)}\right) \cdot \boldsymbol{n}\right] dS,\\
&\boldsymbol{M}_v = \rho \int_V \boldsymbol{H}^T \boldsymbol{H} dV,\\
&{}^{t+\Delta t}\boldsymbol{K}_{vv}^{(i-1)} = \rho \int_V \boldsymbol{H}^T (\boldsymbol{H}\, {}^{t+\Delta t}\boldsymbol{v}^{(i-1)}) \nabla^T \boldsymbol{H} dV,\\
&{}^{t+\Delta t}\boldsymbol{J}_{vv}^{(i-1)} = \rho \int_V \boldsymbol{H}^T (\nabla \boldsymbol{H}\, {}^{t+\Delta t}\boldsymbol{v}^{(i-1)}) \boldsymbol{H} dV,\\
&{}^{t+\Delta t}\boldsymbol{J}_{Tv}^{(i-1)} = \rho c \int_V \boldsymbol{H}^T (\nabla \boldsymbol{H}\, {}^{t+\Delta t}\boldsymbol{T}^{(i-1)}) \boldsymbol{H} dV,\\
&{}^{t+\Delta t}\boldsymbol{K}_{\mu v}^{(i-1)} = \int_V \mu \nabla \boldsymbol{H}^T \nabla^T \boldsymbol{H} dV,\\
&{}^{t+\Delta t}\boldsymbol{K}_{\kappa T}^{(i-1)} = \int_V \kappa \nabla \boldsymbol{H}^T \nabla^T \boldsymbol{H} dV,\\
&{}^{t+\Delta t}\boldsymbol{K}_{\sigma T}^{(i-1)} = \sigma \int_V \boldsymbol{H}^T (\nabla \boldsymbol{H}\, {}^{t+\Delta t}\varphi^{(i-1)}) \nabla^T \boldsymbol{H} dV,\\
&{}^{t+\Delta t}\boldsymbol{K}_{\sigma\varphi}^{(i-1)} = \sigma \int_V \nabla \boldsymbol{H}^T \nabla^T \boldsymbol{H} dV,\\
&{}^{t+\Delta t}\boldsymbol{R}_B = \int_V \boldsymbol{H}^T\, {}^{t+\Delta t}\boldsymbol{f}^{\mathbf{B}} dV,\\
&{}^{t+\Delta t}\boldsymbol{R}_S^{(i-1)} = \int_S \boldsymbol{H}^T \left(-{}^{t+\Delta t}\boldsymbol{p}^{(i-1)} \cdot \boldsymbol{n} + \nabla\, {}^{t+\Delta t}\boldsymbol{v}^{(i-1)} \cdot \boldsymbol{n}\right) dS,
\end{aligned}
\tag{8}
$$

2.3 Boundary conditions

Model has certain limitations [4], [5]. These limitations are included in boundary conditions. It is assumed that:

- the voltage from electrode has a constant value V at the location of damaged cells,
- the voltage on the exterior side of myocardium is zero, which represents a dispersive electrode.
- The initial temperature of myocardium and blood at the start of the analysis is equal 37° C.
- In the case that the blood flows through the coronary artery, the constant value of velocity in the opposite direction of z – axis is v_z= -288 mm/s, which is used from experimental measurement in our previously investigation.
- The components of the blood velocity in x and y directions are equal to zero.

3. Results

The temperature field is calculated for applied voltage of 60V, 30V, 15V, 10V and 14V for all cases to find the best results for desired temperature (50 – 100°C).

3.1 The voltage electrode is 60V

All three cases for voltage electrode of 60V generated temperature fields with higher values of temperature in the marked area. Temperature fields observed in these simulations are shown in the Figure 6.

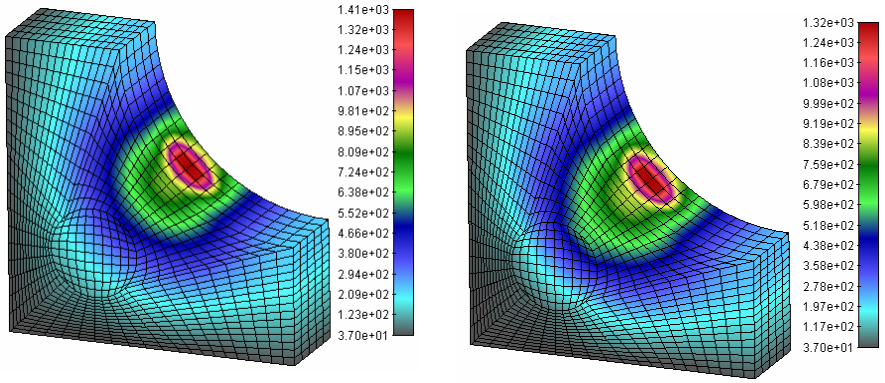

Figure 6. The maximum temperature for the cases when the blood flow is equal to zero (left side of figure) and when there is no blood in the coronary artery (right side of figure) for apllied voltage V=60V after 60s of ablation.

It can be seen from Figure 6 that after 60s of ablation process, temperature of the contact point between electrode and endocardium reaches 1410°C when blood flow through coronary artery is equal to zero. In the case when blood is pumped out from the coronary artery and when air exists in the coronary artery, temperature is lower (1320°C) which is still too high for the ablation process.

As small differences in the maximum temperature for cases when blood flow in the coronary artery is stopped and when blood flows through the coronary artery exists, it is sufficient to analyze only the case when blood flow through the coronary artery is equal zero for all electrode voltage simulations.

A biological heat conduction equation [11] can be written as:

$$\rho c \frac{\partial T}{\partial t} = \nabla \cdot (\kappa \nabla T) + J \cdot E - Q_h \tag{9}$$

where Q_h is the heat loss due to blood flow through myocardium. The term (Q_h) can be considered as negligible during normal ablation process which takes about 60s.

A larger difference in the temperature fields occurs in the case when blood is pumped out from the coronary artery. That is a reason that values of temperature fields are only compared for two cases.

In the case when applied voltage on the electrode is 60V, besides high temperature values there is also a quick response. After only 1s temperature is over 100°C and the ablation process could not be finished.

The instruments for ablation process usually cut energy distribution if the tip electrode reaches temperature over 100°C [4] and for this voltage on the electrode ablation is not possible.
The ablation process needed temperature range of 50 – 100°C, because destroing damaged cells is possible when temperature is over 50°C, and upper bound of 100°C represents temperature which patient can afford during operation [4].
A diagram of temperature versus time at the contact point between electrode and endocardium for electrode voltage of 60V is shown in the Figure 7.

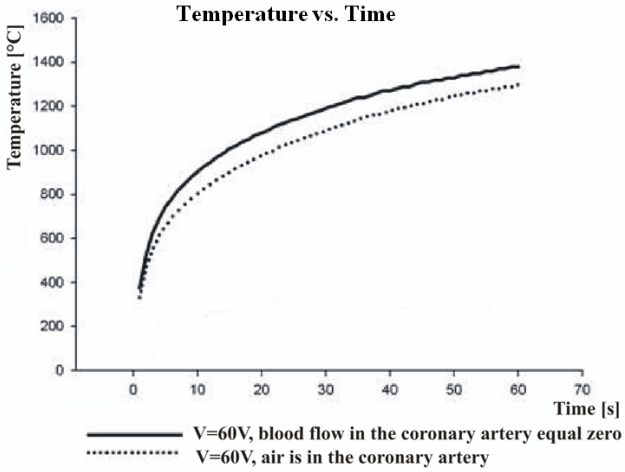

Figure 7. Temperature versus time for electrode voltage of 60V at the contact point between electrode and endocardium during 60s of the ablation process

3.2 The voltage electrode is 30V

When electrode voltage is 60V, simulations show undesirable results because ablation process is impossible even at the start. For that reasons electrode voltage is reduced to 30V. The values of temperature fields for applied voltage of 30V are shown in Figure 8.

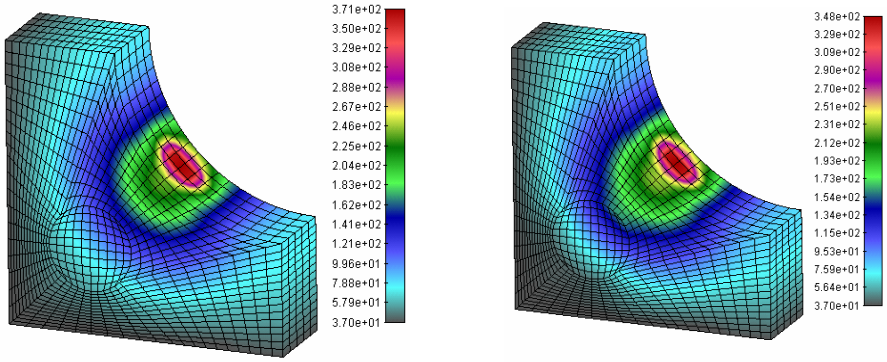

Figure 8. The maximum temperature for the cases when the blood flow equal zero (left side of figure) and when no blood in the coronary artery (right side of figure) for apllied voltage V=30V after 60s of ablation.

In comparison with 60V, when applied voltage is 30V, generated temperature fields have lower values: 371°C when there is no blood flow in the coronary artery, and 348°C when air is in the coronary artery; but the temperature increase is still very fast, and about only 2s after starting ablation temperature exceeds 100°C at contact point between electrode and endocardium.
The temperature versus time diagram is given in the Figure 9.

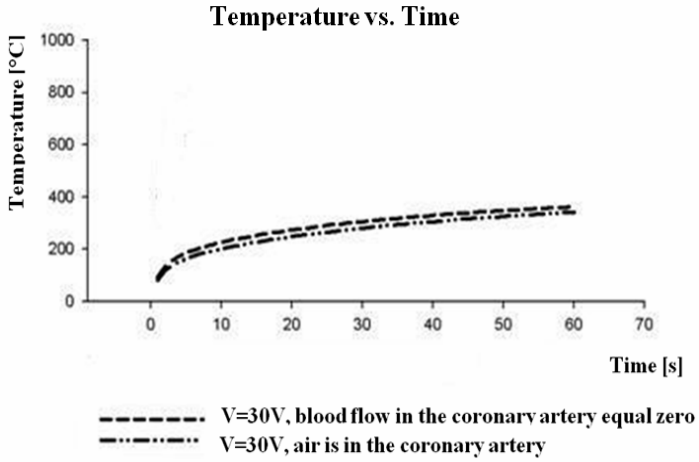

Figure 9. Temperature versus time for electrode voltage of 30V at the contact point between electrode and endocardium during 60s of ablation process

The temperature field is still not in the desirable range, but from simulations with applied voltage on electrode of 60V and 30V it can be concluded that with further reducing of voltage, the conditions for ablation process can be achieved. So, the following simulations are performed with electrode voltage of 15V.

3.3 The electrode voltage is 15V

The calculated temperature field for applied voltage of 15V is in desirable range and it is shown in the Figure 10.

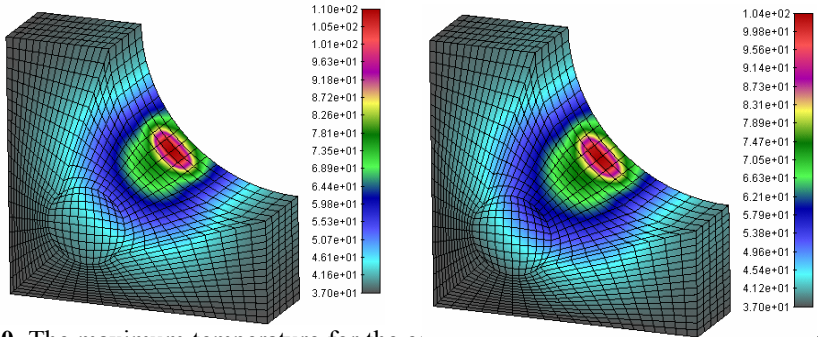

Figure 10. The maximum temperature for the cases when the blood flow is equal zero (left side of figure) and when there is no blood in the coronary artery (right side of figure), after 60s of ablation, for apllied voltage V=15V.

It can be observed from Figure 10 that temperature is in the appropriate range. Quickly after starting ablation the temperature in the damaged cells reaches 50°C. The maximum temperature at electrode tip after 60s of ablation process is 110°C in the case when blood flow through the coronary artery is equal to zero, and 104°C when in the coronary artery is air. The temperature exceeds a critical temperature of 100°C and it is necessary to stop ablation process before 60s is expired.

The temperature versus time diagram for applied voltage of 15V is given in the Figure 11.

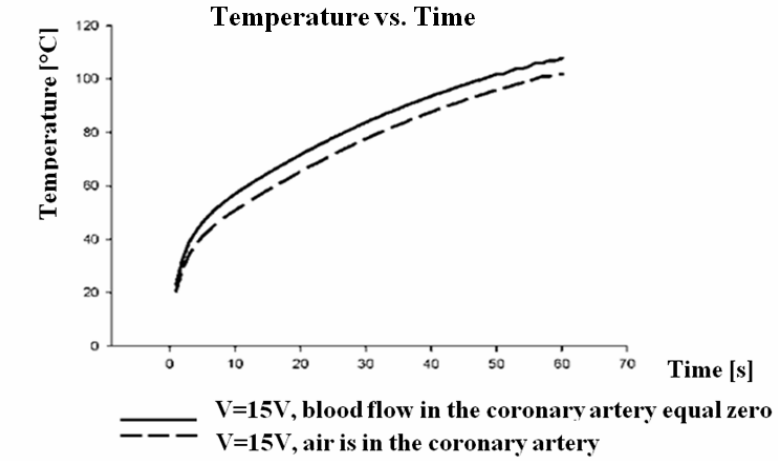

Figure 11. Temperature versus time for electrode voltage of 15V at the contact point between electrode and the endocardium during 60s of ablation process

It can be observed from Figure 11 that positive effects of ablation process can be achieved after 6s when blood flow is stopped in the coronary artery, i.e. after 9s when in the coronary artery is air. At these moments temperature reaches 50°C and the real ablation starts. The process continues until 47s from the beginning, if blood velocity in the coronary artery is equal to zero, and 55s for the case when in the coronary artery is air.
The time period for ablation is large enough, temperature has rapid increase and exceeds for a small value the critical temperature of 100°C.
For better patient security, it is desirable to stop ablation process before the temperature reaches critical value, or to ensure that temperature never reaches the critical value. In that case it is necessary to further reduce voltage of the electrode. For this reason, generated temperature fields were calculated for applied voltage electrode of 10V.

3.4 The electrode voltage is 10V

In the case when voltage on the electrode is 10V the results are shown in the Figure 12.

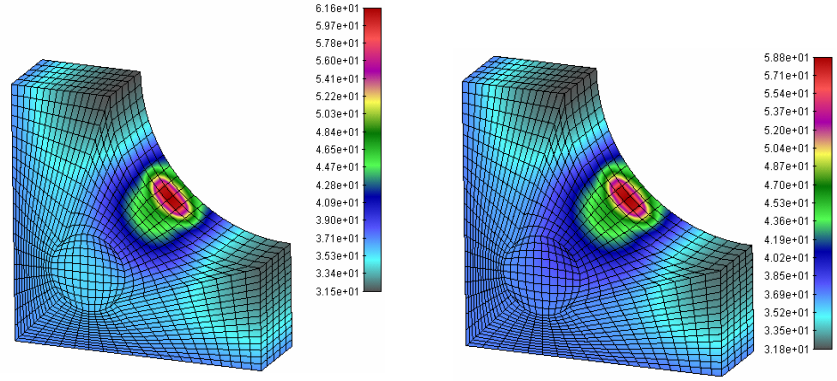

Figure 12. The maximum temperature for the cases when the blood flow is equal to zero (left side of figure) and when there is no blood in the coronary artery (right side of figure) for apllied voltage V=10V, after 60s of process ablation

The maximum temperature at the contact point between electrode and the endocardium is a bit higher than 50°C. Temperature do not reach or exceed the critical temperature. Process is safe for the patient, but the time when ablation shows positive effect is shortened to 10s. It is necessary 50s to exceed 50°C which can be seen in Figure 13.

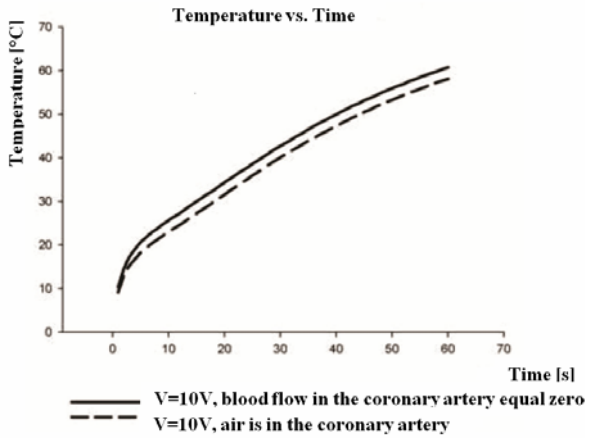

Figure 13. Temperature versus time for electrode voltage of 10V at the contact point between electrode and endocardium during 60s of ablation process

If the voltage is decreased for 5V, then it is below necessary value for successful ablation process. Because of that, we considered the case when electrode voltage is 14V.

3.5 The electrode voltage is 14V

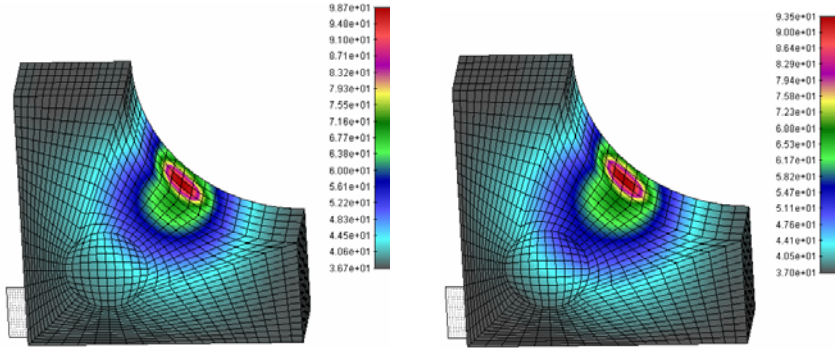

Figure 14. The maximum temperature for the cases when the blood flow is equal to zero (left side of figure) and when there is no blood in the coronary artery (right side of figure) for apllied voltage V=14V, after 60s of ablation process

For electrode voltage of 14V, temperature does not exceed the critical temperature (100°C) so there is no danger for a patient life. In the case when there is no blood flow in the coronary artery, after 60s of ablation process the maximum temperature is 98.7°C, and for the case when air is inside the coronary artery - it is 93.5°C.
A drawback for these simulations is a long time period until starting ablation heat destroying, about to 10s or 14s, which is shown in the Figure 15 for two cases, respectively.
.

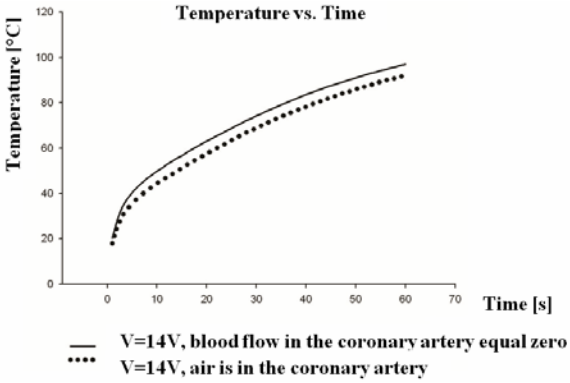

Figure 15. Temperature versus time for voltage electrode of 14V at the contact point between electrode and the endocardium during 60s of ablation process

The appropriate results were obtained for electrode voltage 14V and 15V. In the selection criteria the critical temperature and the temperature increase rate are important. If it is necessary to have a rapid temperature increase, with considerable temperature values, electrode voltage of 15V should be used. On the other hand, if it is required that temperature do not exceed critical temperature of 100°C with considerable slow temperature increase, electrode voltage 14V should be used.

The differences are small between cases when the blood flows through the coronary artery and when there is no blood flow. The blood flow decreases temperature in the range of 0.1-0.01, which is not a significant effect on the maximum temperature.

The obtained results are given in Table 3:

	contact electrode-endocardium		point inside the myocardium		point inside the coronary artery	
time	v=0mm/s	v=288mm/s	v=0mm/s	v=288mm/s	v=0mm/s	v=288mm/s
1	23.4	23.4	20.9	20.9	0.635	0.634
2	33.2	33.3	26.4	26.4	2.02	2.02
3	39.1	39.2	28.7	28.7	3.93	3.93
4	43.2	43.3	30	30	6.08	6.08
5	46.4	46.5	30.9	30.9	8.26	8.26
6	49.1	49.2	31.5	31.5	10.4	10.3
7	51.4	51.5	31.9	31.9	12.3	12.3
8	53.4	53.6	32.3	32.3	14.1	14.1
9	55.3	55.4	32.6	32.6	15.7	15.7
10	57.1	57.2	32.9	32.9	17.2	17.2
11	58.8	58.9	33.1	33.1	18.5	18.5
12	60.4	60.5	33.3	33.3	19.8	19.8
13	61.9	62	33.5	33.5	20.9	20.9
14	63.4	63.5	33.6	33.6	21.9	21.9
15	64.9	65	33.8	33.8	22.9	22.8

Table 3 Temperature differences for the cases when there is no blood flow and when the blood flows with velocity of 288 mm/s through the coronary artery, at characteristic points for the first 15s of ablation and applied voltage V=15V.

4. Conclusions

Endocardial ablation is a new medical procedure which with a significant probability removes heart arrhythmia illness. Thanks to heat, which is generated around electrode, cells which cause irregularity of heart beats are destroyed and regular electrical heart conduction pathways are again established.
Ablation is faster and more secure than surgical operations and can be applied when surgical operation is not possible to perform. It is very important to know distribution of generated temperature field, maximum temperature at the contact between electrode and heart (which must not exceed critical value of 100°C), dimensions of lesion, surface covered with cells destroyed in ablation process (damaged and surrounding healthy). Standard procedure is taking about 60s and in that interval maximum temperature must be in the range of 50°C – 100°C. In the presented simulations, with use of a specific model, it

was found that appropriate temperature fields were generated in the case when electric voltage is 14V and 15V. To reduce temperature at contact point during epicardial ablation saline can be used for cooling. Lower temperatures will be observed if model includes blood flow through the heart, because blood will carry away the thermal energy.
In this study the temperature distribution through the heart was calculated, and it was investigated how temperature depends on electrode's voltage and the blood flow in the coronary artery. It is concluded that temperature increases with increase of applied electrode voltage, temperature rapidly reaches 100° C, and makes ablation process shorter. Blood flow in the coronary artery has no significant influence on the maximum temperature and time of ablation. Much more effects can be reached if blood is pumped out from the coronary artery.

Acknowledgements

The authors acknowledge support of the Ministry of Science of Serbia, grants ON174028 and III41007.

References

[1] www.wikipedia.org
[2] Cao H, Tsai J Z, Choy Y B (2001) "Flow Effect on Lesion Formation in RF Cardiac Catheter Ablation", **48**.
[3] Majerović (2002) "Novi način lečenja metastatskih tumora", *VJESNIK*.
[4] Jain M K, Wolf P D (2000) "A Three Dimensional Finite Element Model of Radiofrequency Ablation with Blood Flow and its Experimental Validation", **28**, pp. 1075-1084.
[5] Gopalakrishnan J (2002) "A Mathematical Model for Irrigated Epicardial Radiofrequency Ablation", **30**, pp. 884-893.
[6] Cao H, Speidel M A, Tsai J Z, et al (2002) "FEM Analysis of Predicting Electrode – Myocardium Contact From RF Cardiac Catheter Ablation System Impedance", **49**.
[7] Filipović N, (1999) "Numerical Analysis of Coupled Problems: Deformable Body and Fluid Flow", Ph. D. Thesis, University of Kragujevac, Serbia,Gentile F, Chiappini C, Fine D, Bhavane RC, Peluccio MS, Ming-Cheng Cheng M, Liu X, Ferrari M.
[8] Filipović N, Kojić M, (2004) "Computer simulations of blood flow with mass transport through the carotid artery bifurcation", *Theoret. Appl. Mech. (Serbian)*, **31**, pp. 1-33.
[9] Kojić M, Filipović N, Stojanović B, Kojić N, (2008) "Computer Modelling in Bioengineering – Theoretical Background, Examples and Software", J. Wiley and Sons.
[10] Obradović, M., Avilla A., Thiagalingam, A. and Filipović N, „Finite element modeling of the endocardial radiofrequency ablation", *J. Serbian Society for Computational Mechanics*, **4**, 2, 43-53, 2010.
[11] Cao H, et al (2002) "Using Electrical Impedance to Predict Catheter – Endocardial Contact During RF Cardiac Ablation", **49**.

DPD MODELING OF INHIBITION PROCESS OF COROSION PROTECTION USING NANOCONTAINERS

D. Petrovic[1,2], M. Obradovic[1,2], A. Jovanovic[3], S. Jovanovic[3], D. Balos[3], M. Kojic[1,4] and N. Filipovic[1,2]

[1]Research and Development Center for Bioengineering, BioIRC, Kragujevac, Serbia
e-mail: racanac@kg.ac.rs
[2]Faculty of Mechanical Engineering, University of Kragujevac, Serbia
e-mail: fica@kg.ac.rs
[3]Risk-technologies, GmbH, Stuttgart, Germany
e-mail: jovanovic@risk-technologies.com
[4]Methodist Hospital Research Institute, Houston, USA
e-mail: mkojic@hsph.harvard.edu

Abstract. Biological systems have the ability to heal wounds and this analogy could also be applicable in materials damage. The surface defects of the material are difficult to detect and difficult to repair. Recent research of the nanocontainers with process of self-healing materials promises a good avenue for new smart nanocoating interfaces. We use Dissipative Particle Dynamics (DPD) computer modeling method to investigate coating substrates that contain nanoscale defects with healing agents.The numerical modeling uses the three usual DPD forces: repulsive, dissipative and random forces, as well as additional forces which bound healing agents to metal substrate. The initial results show the process of protection of metal surface which is treated with these healing agents. Further application of DPD modeling coupled with risk assessment technology could help faster development of new active multi-level protective systems for future vehicle materials.

1. Introduction

Small size defects can appear on a material surface. Such defects have a substantial effect on the mechanical properties of material. To protect this material failure the coating systems are employed on a wide range of engineering structures, from cars to aircrafts, from chemical factories to household equipment. The “self-healing” or “inhibition” are a relatively new terms in material science which means a self-recovery of initial properties of the material after destructive actions of external environment. It is an urgent demand for industrial applications to initiate development of an active healing mechanism for polymer coatings and adhesives.

2. DPD Model

The coating layer with nanoscopic noach can be modeled using molecular dynamics [1]. Another approach to this problem is a mesoscoping modeling using the DPD method [2], [3]. Motion of each DPD particle (further called “particle”) is described by the following Newton law equation:

$$m_i \dot{\mathbf{v}}_i = \sum_j \left(\mathbf{F}_{ij}^C + \mathbf{F}_{ij}^D + \mathbf{F}_{ij}^R \right) + \mathbf{F}_i^{ext} \tag{1}$$

where m_i is the mass of particle "*i*"; $\dot{\mathbf{v}}_i$ is the particle acceleration as the time derivative of velocity; $\mathbf{F}_{ij}^C$, $\mathbf{F}_{ij}^D$, and $\mathbf{F}_{ij}^R$ are the conservative (repulsive), dissipative and random (Brownian) interaction forces, that particle "*j*" exerts on particle "*i*", respectively, provided that particle "*j*" is within the radius of influence r_c of particle "*i*"; and $\mathbf{F}_i^{ext}$ is the external force exerted on particle "*i*", which usually represents gradient of pressure or gravity force as a driving force for the fluid domain [4]. The total interaction force $\mathbf{F}_{ij}$ (Fig. 1) between the two particles is

$$\mathbf{F}_{ij} = \mathbf{F}_{ij}^C + \mathbf{F}_{ij}^D + \mathbf{F}_{ij}^R \tag{2}$$

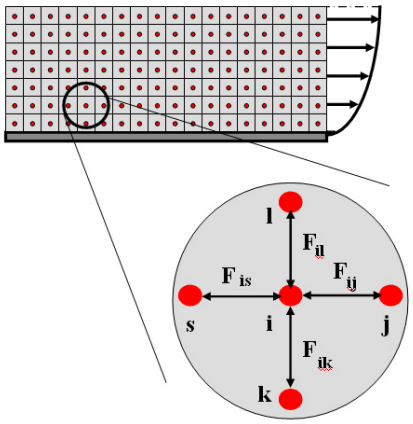

$$\mathbf{F_{ij}} = \mathbf{F_{ij}^{Conservative}} + \mathbf{F_{ij}^{Disipative}} + \mathbf{F_{ij}^{Random}}$$

Figure 1. Interaction forces in the DPD method

The component forces can be expressed as [5]

$$\begin{aligned} \mathbf{F}_{ij}^C &= a_{ij}\left(1-\frac{r_{ij}}{r_c}\right)\mathbf{r}_{ij}^0 \\ \mathbf{F}_{ij}^D &= -\gamma w_D\left(\mathbf{v}_{ij}\cdot\mathbf{e}_{ij}\right)\mathbf{r}_{ij}^0 \\ \mathbf{F}_{ij}^R &= \sigma w_R \xi_{ij}\mathbf{r}_{ij}^0 \end{aligned} \tag{3}$$

In equation (3), a_{ij} is the maximum repulsion force per unit mass, r_{ij} is the distance between particles *i* and *j*, $\mathbf{r}_{ij}^0 = \frac{\mathbf{r}_{ij}}{r_{ij}}$ is the unit vector pointing in direction from *j* to *i*, γ stands for the friction coefficient, and σ is the amplitude of the random force. Also, w_D and w_R are the weight functions for dissipative and random forces, dependent on the distance *r* from the particle *i*; and ξ_{ij} is a random number with zero mean and unit variance. The interaction

force is equal to zero outside the domain of influence, r_c (Cut Radius), hence $F_{ij} = 0$ for $r_{ij} > r_c$.

Further, in order that a DPD fluid system possess a Gibbs–Boltzmann equilibrium state, the following relation between the amplitudes of the weight functions of dissipative and random forces, w_D and w_R, must hold:

$$w_D = w_R^2 \tag{4}$$

Also the amplitude of the random force σ is related to the absolute temperature T,

$$\sigma = \left(2k_B T\gamma\right)^{1/2} \tag{5}$$

where k_B is the Boltzmann constant. The weight functions can be expressed in a form given as [4]

$$w_D = \left(1-\frac{r_{ij}}{r_c}\right)^2, \quad w_R = 1-\frac{r_{ij}}{r_c} \tag{6}$$

The particles used in this study represent both inhibition agents and surrounding coating material with different material characteristics. This was achieved by taking into account different repulsion force coefficient a_{ij}. The additional interaction forces between particles of inhibition agents, which are placed in the primer layer and metal substrate particles, are added similarly as it was done in a model of thrombosis in [6], [7]. These attractive forces are expressed as

$$F_a = k_{sf}\left(1-\frac{L_{sf}}{L_{sf}^{\max}}\right) \tag{7}$$

where L_{sf} is the distance of the inhibition particle from the substrate, k_{sf} is the effective spring constant, and $L_{sf}^{\max}$ is the maximum length of inhibition particle attractive domain.

3. Simulation Models

3.1 Model with inhibitors in the primer layer

The primer layer is represented by the green particles, while inhibitors are shown as red particles (see Fig. 2). The material is scratched and it should be protected; the scratched domain is represented by grey particles. Water which enters into the scratch is modeled by surrounding light blue particles.

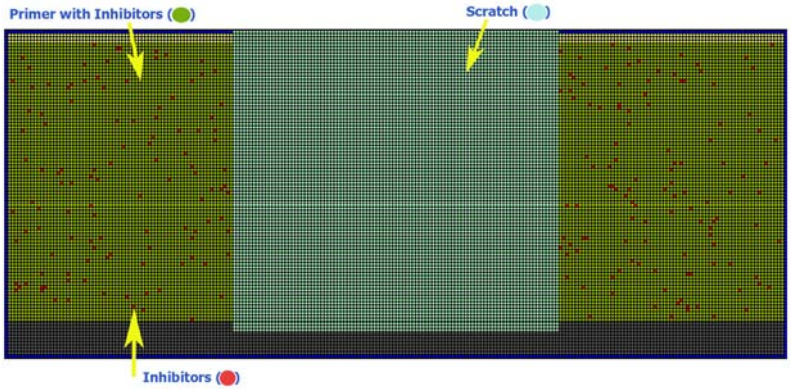

Figure 2. Model of material protection using inhibitors in the primer layer

A graphic interface for modeling, with input parameters that can be changed using dialog window, is shown in Fig. 3.

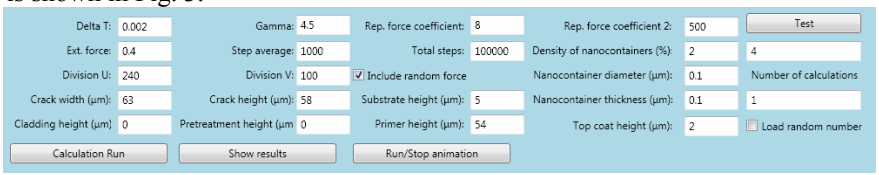

Figure 3. Dialog of the input parameters interface for a 2D DPD modeling. **DeltaT** is the time step for DPD simulation; **Ext. force** is the external force which acts in Y direction on all particles to produce motion; **Division U** is the total number of particles in X direction at initial time; **Division V** is the total number of particles in Y direction at initial time; **Gamma** is the viscosity friction coefficient used in DPD equations; **Step average** is the total number of steps for writing results for animation; **Total steps** is the total number of time steps for the entire modeling period; **Rep. force. coefficient** is the repulsive force coefficient used for repulsive force for simple DPD particles; **Rep. force. coeff. 2** is the repulsive force coefficient used for the repulsive force between inhibition particles; **Include random force** checking button is used for including/excluding random force in a DPD calculation; **Density of Nanocontainers** means percent of inhibition particles in the primer layer; **Calculation** button starts the program execution; **Run/Stop animation** button is used for start/stop animation which is obtained from the DPD calculated results.

The external force is assumed to act on all particles. User can specify a DPD domain by defining a number of particles in X and Y directions. The basic material DPD constants: viscosity friction and repulsive force coefficient, are also prescribed. An additional repulsive force coefficient is given for inhibition particles in order to keep them close and direct them into the surrounding structural matrix which contains simple DPD particles, like primer and scratch particles.
Geometrical parameters of the model are marked in Fig. 4. A scaled model was used for simulation due to a large number of the particles in the real model.

Figure 4. Initial state and dimensions of a real model

In the process of primer protection when the scratch occurred, the inhibitors in the primer layer start to interact with the surrounding particles and slip through the scratch on the metal substrate. For pure protection of metal substrate it is necessary to cover surface with one layer of inhibitors whose diameter is about 1nm. During the process of protection, inhibitor particles interact with primer and fluid particles, but with different repulsive force coefficient ("Rep. force coefficient" and "Rep. force coefficient 2", Fig. 3). Additional spring force was used (equation 7) to connect inhibition with metal substrate particles, so the inhibitors particles are attached to the walls of the crack.

3.2 Model with nanocontainers in the primer layer

Another model was created using nanocontainers which are placed in the primer layer. The initial process of nanocontainer breaking starts at the random position where a crack occurred. The nanocontainer membrane is approximated by one layer of particles and particles inside the nanocontainers represent healing agents – inhibitors. We consider that nanocontainers are fixed in the coating layer (pretreatment or primer layer) so the membrane particles are fixed in the DPD space domain, as can be seen in Fig. 5.

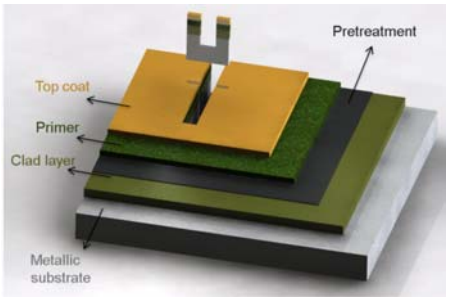

Figure 5. Model with nanocontainers in primer layer

In this model, nanocontainers release the "self – healing" agent particles which are filling the space inside a crack in order to bond it and to protect it from further propagation. We modeled a process of self-healing without additional spring force which we used in the previous model (this force acts between particles themselves and also with respect to those

attached to the walls of the crack - by using equation (7)). Instead of that, we used principle of surface wetting to attach healing agent particles to the damaged metal surface.

4. Results and discussion

We examined two different models. For the first model, with inhibitors in the primer layer, a 2D rectangle crack domain with depth of 0.1 mm was modeled. Total number of DPD particles was 24 000 (240x100) and the model is scaled four times. The total number of time steps for simulation was 100 000.

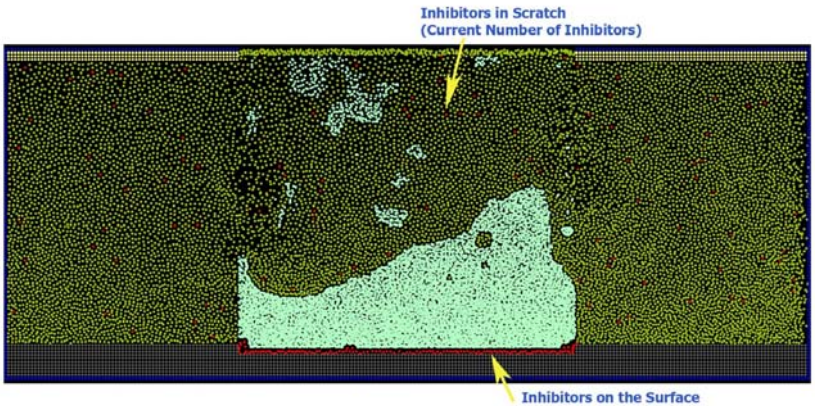

Figure 6. Simulation model after 100 000 time steps (200s). Red particles represent the inhibition particles, green particles make primer layer, grey particles (substrate) are considered to be fixed in space domain. The surrounding particles are shown with light blue color and represent the fluid

A real scenario of realizing inhibition agents is to assume particle motion inside the crack domain and some surrounded area.
We investigated substrate surface coverage and number of inhibitors in the primer needed to protect damaged material and repair it completely.
We tested metal coverage with different percent of inhibitors in the primer: 10%, 15% and 20%. The computed results for the current number of inhibitors in the crack and percentage of covered damaged surface after 200s are given in Fig. 7 and Fig. 8.

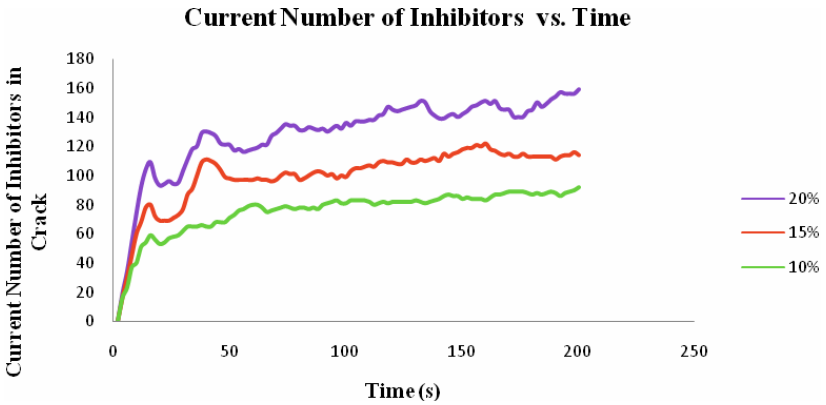

Figure 7. Increase of number of inhibitors on the metal surface during time period obtained by a simple 2D analysis. Total time steps for DPD calculation was 100 000

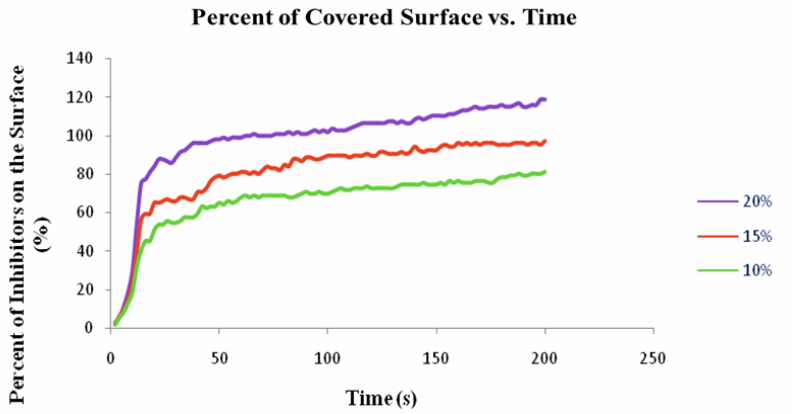

Figure 8. Percentage of inhibitors particles on the metal surface during time period

For the second model, with nanocontainers in the primer layer, we also used a scaled model, shown in Fig. 9.

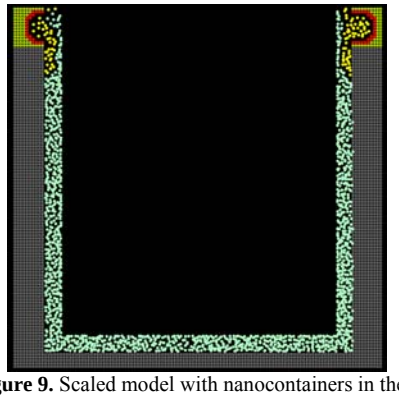

Figure 9. Scaled model with nanocontainers in the primer layer

In the second model we investigated number of nanocontainers which are necessary to completely cover a certain determined surface, and the volume percentage of inhibitors in the nanocontainers. The production of nanocontainers and inhibitors is too expensive and it is needed to precisely establish minimum percentage of inhibitors in the nanocontainers for full protection of the treated material.

We are currently working also on the development of model using Finite Element Method (FEM), for matching results between these two methods (DPD and FEM). The very first results using FEM are shown in Fig. 10.

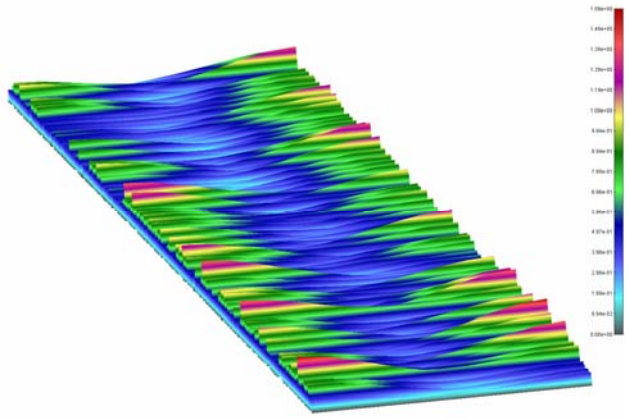

Figure 10. Diffusion of inhibitors on the scratch surface. The width of the scratch is 0.1mm and the length is 100mm.

5. Conclusions

In this study we used DPD and FEM computer modeling methods to investigate coating by the healing agents of substrates that contain nanoscale defects. For the first investigated model it was sufficient to have 20% inhibitors in the primer layer to completely protect the damaged material. By changing the input parameters it was possible to reduce this percentage, but not significantly. In the second model we searched to more reduce this percentage, and for that purpose a DPD model with nanocontainer in the primer layer and FEM model were developed.

Future work will include design of multiple nanocontainers with assumed "density" in the given regions. We also will analyze a coupling of this modeling and a risk assessment technology, which could help faster development of new active multi-level protective systems for future industrial materials.

Acknowledgement. This research was supported by Ministry of Science in Serbia, ON174028, III41007 and FP7 MUST project NMP3-LA-2008-214261.

References

[1] Tyagi S, Lee J Y, Buxton G A, Balazs C A (2004) Using Nanocomposite Coatings To Heal Surface Defects, *Macromolecules*, **37**, pp. 9160-9168.

[2] Filipovic N, Ravnic D J, Kojic M, Mentzer S J, Haber S, Tsuda A (2008b) Interactions of Blood Cell Constituents: Experimental investigation and Computational Modeling by Discrete Particle Dynamics Algorithm, *Microvascular Research*, **75**, pp. 279-284.

[3] Groot R D and Warren P B (1997) Dissipative particle dynamics: Bridging the gap between atomistic and mesoscopic simulation, *J. Chem. Phys.,* **107(11)**, pp. 4423-4435.

[4] Boryczko K, Dzwinel W, Yuen D (2003) Dynamical clustering of red blood cells in capillary vessels, *J. Mol . Model*, **9**, pp. 16-33.

[5] Filipovic N, Kojic M, Tsuda A (2008a) Modeling thrombosis using dissipative particle dynamics method, *Phil Trans Royal*, **366**, pp. 3265-3279.

[6] Hoogerbrugge P J and Koelman J M V A (1992) Simulating microscopic hydrodynamic phenomena with dissipative particle dynamics, *Europhys. Lett.,* **19**, pp. 155-160.

[7] Jovanovic A and Filipovic N (2006) Innovative modelling methods in damage assessment: application of dissipative particle dynamics to simulation of damage and self-healing of polymer coated surfaces, *J. Theoretical and Applied Mechanics*, **44**, pp. 637-648.

DATA MININIG APPLICATION IN THE WALL SHEAR STRESS DISTRIBUTION PREDICTION FOR ANEURYSM AND CAROTID BIFURCATION MODELS

M. Radovic[1,2], D. Petrovic[1,2], and N. Filipovic[1,2]

[1] Bioengineering Research and Development Center, BioIRC Kragujevac
Prvoslava Stojanovica 6, 34000 Kragujevac
e-mail: mradovic@kg.ac.rs, racanac@kg.ac.rs
[2] Faculty of Mechanical Engineering, University of Kragujevac
Sestre Janjic 6, 34000 Kragujevac
e-mail: fica@kg.ac.rs

Abstract. It is well known that there is arterial geometry variability within and across individuals. Computer modeling are used for investigation of geometric parameters, blood density, dynamic viscosity, blood velocity and wall shear stress (WSS) distribution in the human carotid artery bifurcation and aneurysm. In this study two prediction models for evaluating the computer model parameters are used: neural network model and k-nearest neighbor model. The results show that both models have high prediction ability for this prediction task. The high speed calculation with data mining algorithms has a potential benefit for clinical diagnostics in real time using a given patient data.

1. Introduction

A mechanical quantity characteristic for the blood-wall interaction is the wall shear stress, which also has direct physiological effects on the endothelial cell behavior. Therefore, it is very important to have an insight into the blood flow and shear stress distribution when an aneurism is developed in order to help correlating the mechanical conditions (blood flow and shear stresses) with the pathogenesis on the blood vessels. Also, carotid bifurcation stenosis is a significant cause of stroke, producing the infarction in the carotid region by embolization or thrombosis at the site of narrowing. There are many factors which increase the stroke risk like age, systolic and diastolic hypertension, diabetes, cigarette smoking, etc. It has been shown that changes of the geometrical vessel dimensions in the region of the carotid artery bifurcation certainly affect the blood flow and may lead to stenosis process [1].

There are many studies for steady and pulsatile flow in the human carotid artery [2]-[4]. Wall shear stress (WSS) has been identified to play a major role in the progression of atherosclerosis [5].

Kolachalama used Bayesian Gaussian process emulator to access the relationship between geometric parameters and Maximal Wall Shear Stress (MWSS) and to obtain geometries having maximum and minimum values of the output MWSS [6]. MWSS is important because high value can cause damage of endothelium, while on the other hand a small value can cause atherosclerosis initialization and development.

The rupture of aneurysm, a localized blood-filled balloon-like bulge in the wall of a blood vessel, can cause severe hemorrhage, other complications or death. It has been shown that aneurysm growth occurs at regions of low wall shear stress [7].
In the present work, we evaluate two data mining prediction models (neural network model and k-NN model) and test their performance in modeling the relationship between geometric factors, blood density, dynamic viscosity and blood velocity, and WSS distribution. The basic idea is to construct probabilistic models for the input variables which will replace classical CFD calculations and to give the output parameters of interest very quickly. Motivation for this work is a need for prediction tool in clinics which can be run in real time.
The present approach can be viewed as a computer-based data mining strategy which extracts useful information and synthesizes interesting relationships from data sets generated by performing computer modeling on selected cases. The human carotid artery bifurcation and abdominal aortic aneurysm were chosen for this analysis.

2. Methodology

2.1. Data Sets for Modeling WSS Distribution

To demonstrate applicability of data mining techniques for assessing relationships between geometric parameters, density, viscosity, input velocity and wall shear stress (WSS) distribution, data sets containing 4779 different examples are created for both abdominal aortic aneurysm and carotid bifurcation models. Tables 1 and 2 show the mean values of input variables for two different Finite Element Method (FEM) models. The perturbation of each parameter was taken as 30% of the corresponding mean value.

Table 1. The Average Values of Input Parameters for the Abdominal Aortic Aneurysm Model

Description	Mean value	Unit
Length	100	mm
Aneurysm length	40	mm
A	30	mm
Aorta diameter	20	mm
C	20	mm
B	20	mm
Density	0.00105	g/mm^3
Dynamic viscosity	0.003675	Pa·s
Velocity	28.13	mm/s

Table 2. The Average Values of Input Parameters for the Carotid Bifurcation Model

Description	Mean value	Unit
Angle ICA-CCA	25	degree
Angle ECA-CCA	25	degree
Diameter of CCA	6.2	mm
Diameter of CBRE	3.658	mm
Diameter of CBRI	4.9	mm
Length of CCA	7.44	mm
Length of CBR	7.316	mm
Length of ECA	18.6	mm
Length of ICA	26.04	mm
Diameter at end of ICA	4.34	mm
Diameter of ICB	6.49	mm
Distance to ICB	5.39	mm
Density	0.00105	g/mm
Dynamic viscosity	0.00367	Pa·s
Velocity	233	mm/s

Geometric parameters which define geometry of the abdominal aortic aneurysm model and the carotid bifurcation model are shown in Figures 1 and 2, respectively. It can be seen from these figures that the aneurysm model is defined with 6 and the carotid bifurcation model with 12 geometric parameters. With additional blood density, viscosity and maximum velocity as parameters, our data mining models have 9 inputs in case of the abdominal aortic aneurysm and 15 inputs in case of the carotid bifurcation model.

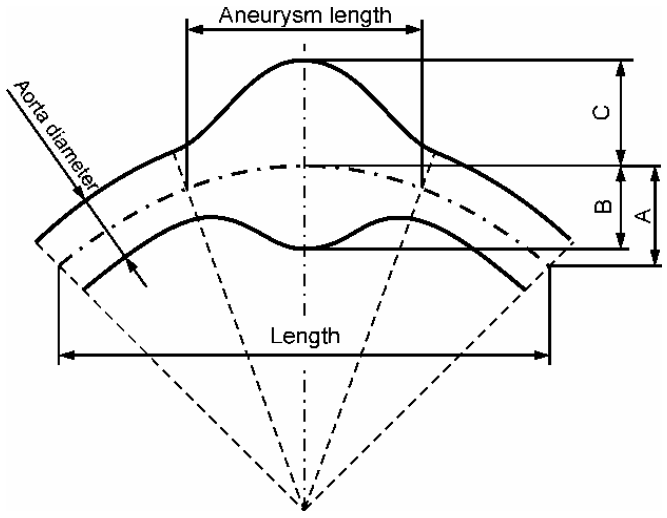

Figure 1. Geometrical parameters of aneurysm model: 'Length' is the parameter which defines the total horizontal projection of the generated aneurysm model; '*A*' is the height of the arc of central line; 'Aorta diameter' is the abdominal aorta diameter; '*B*' is the radius from the central line to the inner wall of the aneurysm; '*C*' is the radius from the central line to the outer wall of the aneurysm; 'Aneurysm length' is an average length of the aneurysm.

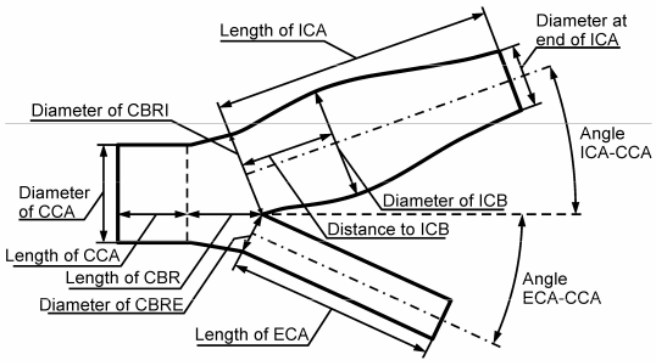

Figure 2. Geometrical data for the carotid artery model. The abbrevations here are: CCA –common carotid artery, CBR – carotid bifurcation region, CBRE – carotid bifurcation region external, ECA- external carotid artery, CBRI- carotid bifurcation region internal, ICA- internal carotid artery, ICB- internal carotid bulbus.

The FEM model of the abdominal aortic aneurysm contains 375 nodes, where 195 nodes represent the surface mesh. On the other hand, FEM model of the carotid bifurcation contains 1854 nodes, with 642 nodes on the surface. By using CFD modeling, WSS values are calculated at the surface nodes, for each of 4779 different geometries of both models. FEM models of the abdominal aortic aneurysm and carotid artery bifurcation are shown in Figure 3.

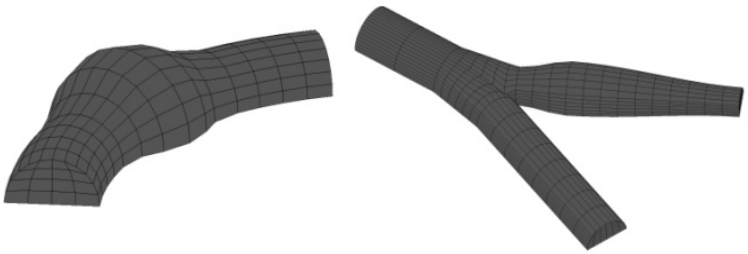

Figure 3. Finite element models of the abdominal aortic aneurysm and the carotid artery bifurcation

2.2. Multilayer Perceptron Neural Network

Multilayer perceptron neural network (MLP) is composed of simple elements called *neurons*. The basic structure of the MLP–consists of one or more hidden layers and an output layer.

The objective of the network training is to find a set of weights and biases that minimizes the error between the neural network predictions and the desired outputs. There are different learning algorithms. The back-propagation algorithm [8] has been the most commonly used training algorithm. On the other hand, the basic algorithm is a gradient descent method in which the network weights and biases are moved along the negative performance function. A single iteration of this algorithm can be written as:

$$\Delta X = lr \cdot \frac{dperf}{dX} \tag{1}$$

where X represents the weight and bias variables of the network, lr is learning rate, and $perf$ is performace function which defines how much real outputs disagree with the predicted ones (mean squared error for example).
This algorithm has problems with local minima and slow convergence. In the literature, a number of variations of the standard algorithm have been developed [9]. In this study we used backpropagation algorithm with momentum and adaptive learning rate. Each variable is adjusted according to gradient descent with momentum:

$$\Delta X = m_c \cdot \Delta X_{prev} + lr \cdot m_c \cdot \frac{dperf}{dX} \tag{2}$$

where m_c is the momentum constant and ΔX_{prev} is the previous change of the weight or bias. For each epoch, if performance decreases toward the goal, the learning rate is increased by the lr_{inc} factor. If performance increases by more than the $\max_{inc}$ factor, the learning rate is adjusted by the factor lr_{dec} and the change that increased the performance is not made. Values of m_c, lr_{inc}, lr_{dec} and $\max_{inc}$ used in the training process are given in table 3.

Table 3. m_c, lr_{inc}, lr_{dec} and $\max_{inc}$ Values Used for Multilayer Perceptron Training

m_c	lr_{inc}	lr_{dec}	$\max_{inc}$
0.9	1.05	0.7	1.04

MLP, with as few as one single hidden layer, is indeed capable of universal approximation of any Borel measurable function in a very precise and satisfactory sense [10].
There are several different criteria for learning stop (maximum number of epochs, maximum amount of time, performance goal, etc.). In this study we used maximum number of learning epochs to be (1000).

2.3. K-Nearest Neighbors Algorithm

K nearest neighbors algorithm (k-NN) belongs to a class of lazy learning methods [11], [12]. When a new example is presented to a nearest neighbor predictor, a subset of learning examples most similar to the new example is used to make a prediction.
For regression problems the mean target variable value from the set of nearest neighbors is predicted:

$$c_x = \frac{1}{k}\sum_{i=1}^{k} c_i \tag{3}$$

where k is the number of nearest learning examples which influence the prediction of k-NN algorithm.
Type of distance measure has a big impact on determining which set of learning examples are closest to the new example. In most cases, Euclidean distance is used:

$$D(t_l, t_j) = \sqrt{\sum_{i=1}^{a} d(v_{i,l}, v_{i,j})^2} \tag{4}$$

where $D(t_l, t_j)$ is the Euclidean distance between 2 examples t_l and t_j, a is the total number of attributes, $v_{i,l}$ is value of *i*-th attribute of *l*-th learning example, and $v_{i,j}$ is value of *i*-th attribute of *j*-th learning example

Before calculating Euclidean distance, all attributes are scaled to the [0,1] interval. For continuous attributes, the distance between two attribute values $v_{i,l}$ and $v_{i,j}$ is defined as:

$$d(v_{i,l}, v_{i,j}) = \left| v_{i,l} - v_{i,j} \right| \tag{5}$$

3. Results

In this study we used multilayer perceptron neural networks trained with backpropagation algorithm and k-nearest neighbor algorithm for predicting wall shear stress distribution for two different FEM models. The problem that we are solving is multi-target prediction problem, and because of that for each surface node of models we created one MLP (see Fig. 4). This means that our model consists of 195 different neural networks in case of the abdominal aortic aneurysm model, and 642 different neural networks in case of the carotid artery bifurcation model, one network for each surface node. For training this model and k-NN model with 70% of total data is used (3346 learning examples). Remaining 30% of data is used for testing (1433 testing examples).

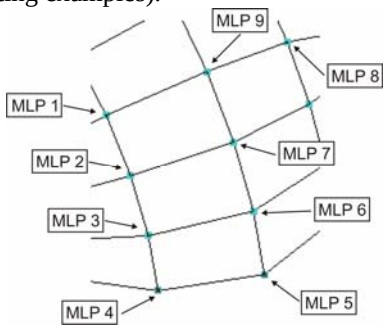

Figure 4. Neural network model – for each node one MLP is created.

Multilayer perceptrons are used with 5 neurons in hidden layer, bipolar sigmoid activation functions in hidden neurons, and linear activation function in the output neuron. The stopping criterion was defined as the maximum number or learning epochs (1000). The number of neurons in the input and output layer is determined by the problem we are solving. Input layer has nine input neurons (in case of aneurysm model) or fifteen input neurons (in case of carotid bifurcation model), corresponding to input parameters (see tables 1 and 2). The output layer consists of one neuron corresponding to WSS value of the node for which neural network is created.

The k-NN model predicts the target values that are averaged from the 5 most similar learning examples (nearest neighbors) in the problem space.

We evaluated performance of the models by computing their relative mean square error (RMSE). The RMSE is computed as a sum of the squared differences between the true and the predicted values of the outputs for all of 1433 testing examples in the data set, normalized afterwards by the sum of the squared errors of the default predictor (i.e. a model which always predicts average values of the outputs).
For a j-th testing example, squared error is given as:

$$ERR_j = \sum_{i=1}^{n} \left(f_{j,i} - \hat{f}_{j,i} \right)^2 \tag{6}$$

where n is the number of surface nodes (195 or 642), $\hat{f}_{j,i}$ is the predicted WSS value for i-th node for j-th example and $f_{j,i}$ is the true value of WSS for i-th node of j-th example.

In the same way, squared error for default predictor (i.e. a model which always predicts an average value of the output) for j-th learning example is given as:

$$\overline{ERR_j} = \sum_{i=1}^{n} \left(f_{j,i} - \bar{f}_i \right)^2 \tag{7}$$

where $\bar{f}_i$ is the average value of WSS for i-th node among training examples:

$$\bar{f}_i = \frac{1}{N_{train}} \sum_{j=1}^{N_{train}} f_{j,i} \tag{8}$$

where N_{train} is the number of training examples (3346).

Finally, RMSE is calculated as:

$$RMSE = \frac{\sum_{j=1}^{N_{test}} ERR_j}{\sum_{j=1}^{N_{test}} \overline{ERR_j}} \tag{9}$$

where N_{test} is the number of testing examples (1433).

The value of RMSE smaller than 1.0 indicates that the model is useful. The lower RMSE is, the more accurate the model is. The RMSE values for the tested models are shown in tables 4 and 5 for aneurysm and carotid bifurcation model, respectively.

Table 4. Relative Mean Squared Error of the Tested Models for Aneurysm Model

Model	RMSE
MLP	0.0351
k-NN	0.1008

Table 5. Relative Mean Squared Error of the Tested Models for Carotid Bifurcation Model

Model	RMSE
MLP	0.0305
k-NN	0.2416

Figures 5 and 6 show calculated and predicted WSS distribution for three randomly chosen

test examples for the abdominal aortic aneurysm and carotid artery bifurcation models.

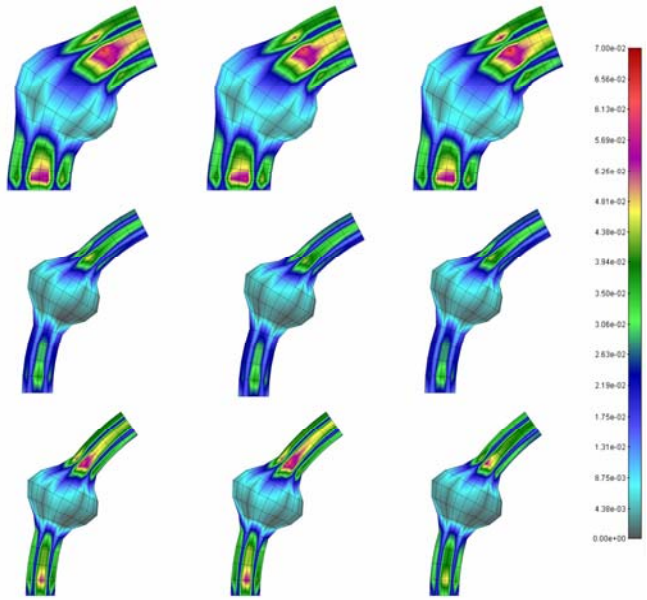

Figure 5. WSS distribution for the abdominal aortic aneurysm model for three randomly chosen test examples: left-calculated, middle-MLP predicted, right-k-NN predicted.

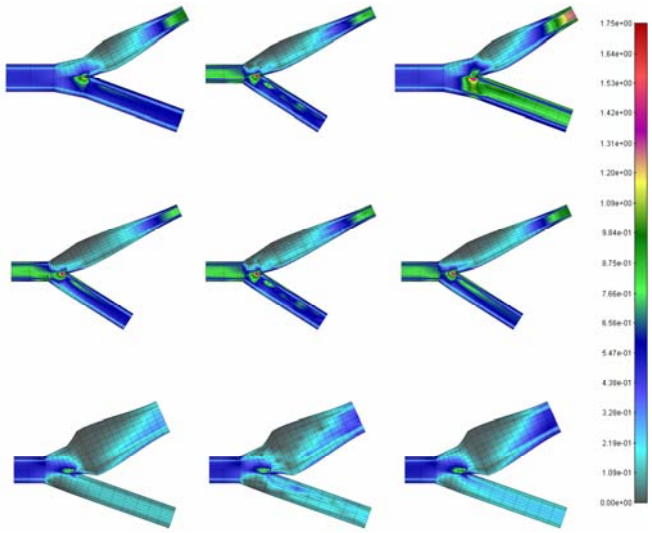

Figure 6. WSS distribution for the carotid artery bifurcation model for three randomly chosen test examples: left-calculated, middle-MLP predicted, right-k-NN predicted.

From tables 4 and 5 we can see that both, neural network and k-NN models, showed high potential in WSS distribution prediction task. The same conclusion follows from Figures 5

and 6, where we can see that calculated and predicted wall shear stress distributions are quite similar. Neural network model showed higher precision in modeling WSS distribution than the k-NN model for both, the carotid artery bifurcation and the abdominal aortic aneurysm models.

4. Conclusion

This work described an application of data mining methodology to a hemodynamic problem in the cardiovascular medicine. The relationship between geometric parameters, blood density, dynamic viscosity, input blood velocity and the wall shear stress distribution for the human carotid artery bifurcation and abdominal aortic aneurysm were modeled. The results obtained from a large number of computer simulations were used as training data to evaluate two different regression models, which both exhibited capabilities for this task. The neural network model showed better results than the k-NN model. The obtained results demonstrate that these models can be used to aid the assessment of the shear stress distribution for a given patient in real time. Further research will focus on the real life situations where applicability of created data mining applications will be tested on real patient data. Coupling the FEM and Data Mining methods can further facilitate the development of predictive diagnostic system for clinical practice.

Acknowledgement This work was supported in part by the European Commission (Project ARTREAT, ICT 224297) and Ministry of Science in Serbia, Grant ON174028 and III41007.

References

[1] U.G.R. Schulz, P.M. Rothwell, “Sex differences in carotid bifurcation anatomy and the distribution of atherosclerotic plaque,” *Stroke*, vol. 32, no. 7, pp. 1525-1531, 2001.
[2] K. Perktold, D. Hilbert, “Numerical simulation of pulsatile flow in a carotid bifurcation model,” *Journal of Biomedical Engineering*, vol. 8, no. 3, pp. 193-199, 1986.
[3] K. Perktold, H. Florian, D. Hilbert, “Analysis of pulsatile blood flow: A carotid siphon model,” *Journal of Biomedical Engineering*, vol. 9, no. 1, pp. 46-53, 1987.
[4] K. Perktold, R.O. Peter, M. Resch, G. Langs, “Pulsatile non-Newtonian blood flow in three-dimensional carotid bifurcation models: A numerical study of flow phenomena under different bifur-cation angles,” *Journal of Biomedical Engineering*, vol. 13, no. 6, pp. 507-515, 1991.
[5] S. Glagov, C. Zarins, D.P. Giddens, D.N. Ku, “Hemodynamics and atherosclerosis Insights and perspectives gained from studies of human arteries,” *Archives of Pathology & Laboratory Medicine*, vol. 112, no. 10, pp. 1018-1031, 1988.
[6] V.B. Kolachalama, N.W. Bressloff, P.B. Nair, “Mining data from hemodynamic simulations via Bayesian emulation,” *BioMedical Engineering OnLine*, vol. 6, no. 47, 2007.
[7] L. Boussel, V. Rayz, C. McCulloch, A. Martin, G. Acevedo-Bolton, M. Lawton, R. Higashida, W.S. Smith, W. Young, D. Saloner, “Aneurysm growth occurs at region of low wall shear stress: Patient-specific correlation of hemodynamics and growth in a longitudinal study,” *Stroke*, vol. 39, no. 11, pp. 2997–3002, 2008.
[8] D.E. Rumelhart, G.E. Hinton, R.J. Williams, “*Learning internal representations by error propagation*,” MIT Press, Cambridge, MA, USA, 1986, pp. 318-362.
[9] S. Haykin, “*Neural Networks: A Comprehensive Foundation*,” Prentice Hall, New Jersey, USA, 1999.
[10] K. Hornik, “Approximation capabilities of multilayer feedforward networks,” *Neural network*, vol. 4, no.2, pp. 251–257, 1991.
[11] I. Kononenko, M. Kukar, "*Machine learning and data mining*," Horwood Publishing Chichester, UK, 2007.
[12] D. Aha, D. Kibler, “Instance-based learning algorithms,” *Machine Learning*, vol. 6, no. 1, pp. 37–66, 1991.